remote sensing

MDPI

Technical Note

Quality Assessment and Observation Error Estimation of Tianmu-1 GNSS Radio Occultation Bending Angle and Refractivity Retrievals

Li Wang [1,2], Shengpeng Yang [1,2,*], Buwei Yao [3] and Li He [2]

[1] Joint Center of Data Assimilation for Research and Application, School of Atmospheric Sciences, Nanjing University of Information Science and Technology, Nanjing 210044, China; 202411010034@nuist.edu.cn
[2] Laboratory of Beibu Gulf National Climate Observatory, Guangxi Research Institute of Meteorological Science, Nanning 530022, China; gx_heli@sina.cn
[3] School of Remote Sensing and Geomatics Engineering, Nanjing University of Information Science and Technology, Nanjing 210044, China; 202513350031@nuist.edu.cn
* Correspondence: yangshengp@nuist.edu.cn

Highlights

What are the main findings?

- In the upper troposphere and lower stratosphere, Tianmu-1 (TM) bending angle/refractivity biases relative to ERA5 (8–30 km), radiosonde (8–25 km), and COSMIC-2 (8–30 km) are within ±0.19%/±0.09%, ±0.40%/±0.21%, and ±0.37%/±0.14%, respectively.
- Three-cornered hat (3CH) estimates reveal height- and latitude-dependent TM RO observation errors, with larger errors in the lower troposphere and the tropics (±30° latitude).

What are the implications of the main findings?

- The small biases in the 8–30 km layer indicate that TM RO bending angle and refractivity retrievals are reliable for upper-tropospheric and lower-stratospheric weather and climate applications.
- The 3CH derived observation error estimates provide a quantitative basis for specifying TM observation errors in numerical weather prediction data assimilation.

Abstract

As China's first commercial low Earth orbit meteorological constellation, Tianmu-1 (TM) radio occultation (RO) provides high-density observations, with approximately 30,000 profiles per day globally, offering new opportunities for research in observationally sparse regions. TM RO bending angle and refractivity retrievals from June to December 2023 are evaluated using ERA5 reanalysis, global radiosonde observations, and COSMIC-2 RO as reference datasets. TM observation errors are further estimated using the three-cornered hat (3CH) method. The results show that, in the upper troposphere and lower stratosphere, TM bending angle biases are within ±0.19%, ±0.40%, and ±0.37% relative to ERA5 (8–30 km), radiosonde (8–25 km), and COSMIC-2 (8–30 km), respectively. The corresponding refractivity biases are within ±0.09%, ±0.21%, and ±0.14%, respectively. Both bending angle and refractivity from TM RO exhibit high accuracy and precision. The observation errors estimated using the 3CH method show a clear latitudinal dependence. The observation errors in the tropics (±30° latitude) are larger than those in the middle and high latitudes. This study quantitatively characterizes the accuracy, precision, and error structure of TM RO bending angle and refractivity, providing a quantitative basis for future quality control and observation error specification in numerical weather prediction data assimilation.

Check for updates

Academic Editor: Gino Dardanelli

Received: 29 June 2026
Revised: 23 July 2026
Accepted: 26 July 2026
Published: 4 August 2026

Copyright: © 2026 by the authors. Licensee MDPI, Basel, Switzerland. This article is an open access article distributed under the terms and conditions of the Creative Commons Attribution (CC BY) license.

Keywords: Tianmu-1 RO; quality assessment; three-cornered hat; bending angle and refractivity bias

1. Introduction

Global Navigation Satellite System (GNSS) radio occultation (RO) is an active remote sensing and limb sounding technique. Since the successful launch of the first experimental satellite, MicroLab1, in 1996 [1], this technique has been widely used in atmospheric sounding. Over the past three decades, several international GNSS RO missions have been successfully implemented. The COSMIC and COSMIC-2 missions, jointly developed by the United States and Taiwan, China, demonstrated the value of GNSS RO for global atmospheric sounding [2,3]. The European MetOp series (MetOp-A, -B, and -C) has provided timely operational GNSS RO observations, contributing significantly to numerical weather prediction [4,5]. Meanwhile, China's FengYun-3 (FY-3) series (FY-3C, FY-3D, and FY-3E) introduced the first GNSS RO sounder compatible with both the BeiDou Navigation Satellite System (BDS) and the Global Positioning System (GPS) [6,7]. RO data possess several unique characteristics, including high vertical resolution, high precision, long-term stability, global coverage, and near all-weather capability with little influence from clouds and precipitation [2,8]. Consequently, RO observations play an important role in climate monitoring [9] and global and regional numerical weather prediction [10,11]. Although many GNSS RO missions have been successfully launched in the past, the application of RO data in meteorology is still limited by low observation density.

In recent years, with the maturation of small-satellite technology, commercial RO missions have emerged and greatly increased the volume of GNSS RO observations. Examples include Spire from the United States [12], Yunyao-1 from China [13], and Tianmu-1 (TM) from China [14]. These missions provide new opportunities for meteorological research. TM is China's first in-orbit RO meteorological sounding constellation compatible with four major GNSSs: BeiDou, GPS, Galileo, and GLONASS. It is also the world's first commercial GNSS remote sensing constellation to realize integrated sensing of land surface, ocean, atmosphere, and ionosphere. It can simultaneously achieve integrated stereo sounding using both GNSS RO and GNSS reflectometry [15]. The constellation provides more than 30,000 RO profiles per day, making it one of the densest atmospheric RO observing systems worldwide [14]. It provides unprecedented opportunities for atmospheric research over data sparse regions, such as plateaus and oceans.

Before the TM RO dataset can be widely used, a rigorous quality assessment is required to ensure its reliability and stability. In previous studies, GNSS RO data have commonly been compared with radiosonde (RS) observations and model analyses to evaluate their precision and accuracy [3,12]. Radiosondes provide high vertical resolution and high accuracy, whereas model analyses provide large-scale atmospheric information. However, radiosonde observations represent point measurements, and model analyses represent grid point averages. In contrast, GNSS RO measurements represent the integrated atmospheric effect along a ray path. Therefore, comparisons among these datasets are inevitably affected by representativeness and collocation errors.

To complement these conventional comparisons, this study also introduces COSMIC-2 RO data as an RO-based reference to evaluate TM RO retrievals. The high accuracy and precision [2,3] and long-term stability [16] of RO data from the COSMIC and COSMIC-2 missions have been confirmed by numerous studies. Stronger satellite antennas, higher sampling rates, and advanced open-loop tracking techniques have significantly improved the signal-to-noise ratio (SNR) and retrieval accuracy of COSMIC-2 compared with COSMIC [3,17].

Therefore, COSMIC-2 RO data are selected to evaluate the quality of TM RO data. Because TM and COSMIC-2 are both GNSS RO datasets, their comparison can reduce part of the inconsistency associated with different observation types and provide an additional measure of the consistency of TM bending angle (α) and refractivity (N) retrievals.

This study aims to evaluate the quality of TM GNSS RO bending angle and refractivity data using the fifth-generation European Centre for Medium-Range Weather Forecasts (ECMWF) atmospheric reanalysis (ERA5), radiosonde, and COSMIC-2 datasets as references, and to estimate TM-specific observation errors using the three-cornered hat (3CH) method for future data assimilation applications. The paper is organized as follows. Section 2 describes the data and methods used in this study. Section 3 evaluates the accuracy and precision of TM RO data through comparisons with ERA5 reanalysis, radiosonde observations, and COSMIC-2 RO data, and further estimates TM observation errors. Section 4 summarizes the main conclusions.

2. Data and Methods

2.1. Data

This study covers the period from June to December 2023. We use RO data from the TM and COSMIC-2 missions. The TM RO data are provided by Aerospace Tianmu (Chongqing) Satellite Science and Technology Co., Ltd. (Chongqing, China). The TM constellation currently consists of 23 operational satellites. The constellation provides more than 30,000 RO profiles per day. The COSMIC-2 RO data are provided by the COSMIC Data Analysis and Archival Center (CDAAC) [2]. The COSMIC-2 constellation was launched on 25 June 2019. Its 24° orbital inclination enables dense atmospheric sounding over the tropical and subtropical regions (within ±45° latitude), providing more than 4000 atmospheric profiles per day. In this study, we use the retrieved bending angle and refractivity data. These data are obtained from the Level-2 atmPrf products, which provide atmospheric profiles without moisture information, in the COSMIC-2 Near Real-Time dataset and the TM RO dataset.

The Integrated Global Radiosonde Archive (IGRA) dataset used in this study is provided by the National Centers for Environmental Information (NCEI) of the National Oceanic and Atmospheric Administration (NOAA). The dataset contains atmospheric state observations, including pressure, temperature, and geopotential height, and other variables, with records dating back to 1905 [18]. The model datasets used in this study include the ERA5 dataset and the National Centers for Environmental Prediction (NCEP) Final Operational Global Analysis (FNL) dataset.

2.2. Forward Operators for Refractivity and Bending Angle

This paper evaluates the quality of TM RO bending angle and refractivity data. Therefore, forward observation operators are required to derive refractivity and bending angles from radiosonde and model data. Refractivity is a function of temperature, atmospheric pressure, and water vapor pressure, and can be calculated as follows [8]:

$$N = 77.6 \cdot \frac{P}{T} + 3.73 \cdot 10^5 \cdot \frac{P_W}{T^2} \quad (1)$$

where P is the pressure (hPa), T is the temperature (K) and P_W is the water vapor pressure (hPa). A one-dimensional (1D) Abel forward observation operator is then applied to the refractivity profiles derived from the model and radiosonde data to calculate the corresponding ray bending angle profiles at the tangent point [19], as given below:

$$\alpha^{1D}(a) = -2a \int_a^{\infty} \frac{1}{n\sqrt{\mu^2 - a^2}} \frac{dn}{d\mu} d\mu \quad (2)$$

where n is the refractive index, related to refractivity through $n = 1 + N{\cdot}10^{-6}$; μ is defined as $\mu = nr$, where r denotes the distance from the local center of curvature of the Earth [20]; and a is the local angular momentum evaluated at the tangent point, given by $a = r_0 n(r_0)$, where r_0 is the tangent point radius and $n(r_0)$ is the refractive index at the tangent point. The local angular momentum is defined as

$$p_\theta = rn(r)sin\varphi \tag{3}$$

where φ is the angle between the local radius vector and the tangent direction of the ray. At the tangent point, $\varphi = 90°$.

2.3. Quality Assessment Method

For the quality assessment of GNSS RO data, the most commonly used approach is to compare GNSS RO data with model or radiosonde data to estimate the accuracy and precision of the GNSS RO data. However, this approach does not account for representativeness errors associated with the different datasets or errors introduced by the observation operators. To reduce the impacts of these uncertainties, we incorporate an additional comparison between TM RO and the internationally recognized, high-quality COSMIC-2 RO data. The evaluation procedure is as follows:

(1) The mean and standard deviation of the fractional differences between COSMIC-2 RO and ERA5, as well as between TM RO and ERA5, are calculated as follows:

$$\mu^{ERA5}_{COSMIC-2/\mathrm{TM}} = \overline{\left(\frac{RO^{COSMIC-2/\mathrm{TM}} - ERA5}{ERA5}\right)} \tag{4}$$

$$\sigma^{ERA5}_{COSMIC-2/\mathrm{TM}} = \sqrt{\frac{\sum_{i=1}^{n}\left(\left(\frac{RO^{COSMIC-2/\mathrm{TM}} - ERA5}{ERA5}\right)_i - \mu^{ERA5}_{COSMIC-2/\mathrm{TM}}\right)^2}{n}} \tag{5}$$

(2) The mean and standard deviation of the fractional differences between COSMIC-2 RO and radiosonde, as well as between TM RO and radiosonde, are calculated as follows:

$$\mu^{RS}_{COSMIC-2/\mathrm{TM}} = \overline{\left(\frac{RO^{COSMIC-2/\mathrm{TM}} - RS}{RS}\right)} \tag{6}$$

$$\sigma^{RS}_{COSMIC-2/\mathrm{TM}} = \sqrt{\frac{\sum_{i=1}^{n}\left(\left(\frac{RO^{COSMIC-2/\mathrm{TM}} - RS}{RS}\right)_i - \mu^{RS}_{COSMIC-2/\mathrm{TM}}\right)^2}{n}} \tag{7}$$

(3) The mean and standard deviation of the fractional differences between TM RO and COSMIC-2 RO are calculated as follows:

$$\mu^{COSMIC-2}_{\mathrm{TM}} = \overline{\left(\frac{RO^{\mathrm{TM}} - RO^{COSMIC-2}}{RO^{COSMIC-2}}\right)} \tag{8}$$

$$\sigma^{COSMIC-2}_{\mathrm{TM}} = \sqrt{\frac{\sum_{i=1}^{n}\left(\left(\frac{RO^{\mathrm{TM}} - RO^{COSMIC-2}}{RO^{COSMIC-2}}\right)_i - \mu^{COSMIC-2}_{\mathrm{TM}}\right)^2}{n}} \tag{9}$$

To reduce the influence of outliers on the estimation of the mean and standard deviation, a biweight quality control method [21] was applied before calculating these statistics.

2.4. Three-Cornered Hat Method

The 3CH error estimation method is based on three datasets with independent errors. It estimates the error of each dataset through intercomparisons among the three datasets [22,23]. Given three datasets, A, B, and C, the error variance of dataset A relative to B is first calculated as

$$\sigma^2_{(A-B)} = \sigma^2_A + \sigma^2_B - 2COV_{err}(A, B) \tag{10}$$

Similarly, the error variances of dataset A relative to C and dataset B relative to C can be calculated. Assuming that the errors of datasets A, B, and C are uncorrelated, the cross-covariance terms can be neglected. The following system of equations can then be derived:

$$\begin{cases} \sigma^2_{(A-B)} = \sigma^2_A + \sigma^2_B \\ \sigma^2_{(A-C)} = \sigma^2_A + \sigma^2_C \\ \sigma^2_{(B-C)} = \sigma^2_B + \sigma^2_C \end{cases} \tag{11}$$

The error variance of dataset A can then be derived as

$$\sigma^2_A = \frac{1}{2}\sigma^2_{(A-B)} + \frac{1}{2}\sigma^2_{(A-C)} - \frac{1}{2}\sigma^2_{(B-C)} \tag{12}$$

Once the $\sigma^2_{(A-B)}$, $\sigma^2_{(A-C)}$ and $\sigma^2_{(B-C)}$ are obtained, the σ^2_A can be estimated by substituting them into Equation (12).

In this study, radiosonde observations, ERA5 reanalysis data, and FNL analysis data are used in different combinations to estimate the observation error variances of bending angle and refractivity from TM and COSMIC-2 RO. Assuming that cross-covariance terms between datasets are negligible compared with the observation errors in a statistical sense, and acknowledging that the datasets are not strictly independent due to shared observational inputs and assimilation constraints, a system of three simultaneous equations can be derived based on Equation (12):

$$\begin{cases} \sigma^2_1 = \frac{1}{2}\sigma^2_{(RO-ERA5)} + \frac{1}{2}\sigma^2_{(RO-RS)} - \frac{1}{2}\sigma^2_{(ERA5-RS)} \\ \sigma^2_2 = \frac{1}{2}\sigma^2_{(RO-FNL)} + \frac{1}{2}\sigma^2_{(RO-RS)} - \frac{1}{2}\sigma^2_{(FNL-RS)} \\ \sigma^2_3 = \frac{1}{2}\sigma^2_{(RO-ERA5)} + \frac{1}{2}\sigma^2_{(RO-FNL)} - \frac{1}{2}\sigma^2_{(ERA5-FNL)} \end{cases} \tag{13}$$

It should be emphasized that the datasets used in this study are not strictly independent. Both ERA5 and FNL are products constrained by overlapping assimilated observations, including radiosonde and satellite data. The independence assumption of the 3CH method is only approximately satisfied. The 3CH Equation (13) is applied to estimate the error variances of the RO observations. To mitigate dependence on any single reference dataset, multiple 3CH combinations are applied. The resulting estimates should therefore be interpreted as effective observation error variances for collocated RO profiles, which include contributions from measurement errors, representativeness errors, forward-model errors, and collocation uncertainties rather than pure instrument errors.

3. Results

3.1. Comparison Between TM and ERA5

Model analyses provide spatially continuous and dynamically consistent large-scale atmospheric fields. They have therefore been widely adopted as reference datasets for evaluating GNSS RO retrievals from various satellite missions, including COSMIC-2 [3], the MetOp series [5], the FY-3 series [7], and Spire [12]. However, comparisons between RO and model data may include representativeness errors because RO measurements

represent limb-integrated information, whereas model analyses are gridded atmospheric fields. To compare RO with the ERA5 reanalysis, we first interpolated the ERA5 atmospheric variables to the corresponding RO profile locations using horizontal bilinear interpolation and vertical cubic spline interpolation. The refractivity and bending angle were then calculated from the interpolated atmospheric variables.

Figures 1 and 2 show the vertical distributions of the mean and standard deviation of the fractional differences between GNSS RO (COSMIC-2 and TM) and ERA5 during 1–8 June 2023, along with the corresponding data count distributions. Figure 1 presents the results for bending angle, $\left(\alpha^{GNSS} - \alpha^{ERA5}\right)/\alpha^{ERA5}$, while Figure 2 presents those for refractivity, $\left(N^{GNSS} - N^{ERA5}\right)/N^{ERA5}$. In the impact height range of 8–30 km, the bending angle biases of COSMIC-2 and TM RO relative to ERA5 reanalysis data range from −0.10% to 0.16% and from −0.19% to 0.04%, respectively. The corresponding mean bending angle biases are 0.01% and −0.07%. The standard deviations of $\left(\alpha^{COSMIC-2} - \alpha^{ERA5}\right)/\alpha^{ERA5}$ and $\left(\alpha^{TM} - \alpha^{ERA5}\right)/\alpha^{ERA5}$ range from 0.90% to 2.81% and from 1.27% to 2.00%, respectively, with mean values of 1.28% and 1.44% (Figure 1a). In the geometric height range of 8–30 km, the refractivity biases of COSMIC-2 and TM relative to ERA5 reanalysis data range from −0.01% to 0.08% and from −0.09% to 0.07%, respectively. The corresponding mean refractivity biases are 0.03% and −0.01%, respectively. The standard deviations of $\left(N^{COSMIC-2} - N^{ERA5}\right)/N^{ERA5}$ and $\left(N^{TM} - N^{ERA5}\right)/N^{ERA5}$ range from 0.57% to 0.89% and from 0.62% to 1.11%, respectively, with mean values of 0.72% and 0.86% (Figure 2a). The slight increase in $\left(\alpha^{GNSS} - \alpha^{ERA5}\right)/\alpha^{ERA5}$ and $\left(N^{GNSS} - N^{ERA5}\right)/N^{ERA5}$ between 15 and 20 km (Figures 1 and 2) is likely related to variations in tropopause height and sharp vertical gradients near the upper troposphere–lower stratosphere transition. The distributions of $\left(\alpha^{GNSS} - \alpha^{ERA5}\right)/\alpha^{ERA5}$ and $\left(N^{GNSS} - N^{ERA5}\right)/N^{ERA5}$ for COSMIC-2 RO are more concentrated than those for TM RO (Figure 1b,c and Figure 2b,c) in the 8–30 km height range. These results indicate that TM RO retrievals are broadly consistent with ERA5 in the upper troposphere and lower stratosphere, although the fractional difference distributions of COSMIC-2 are generally more concentrated than those of TM.

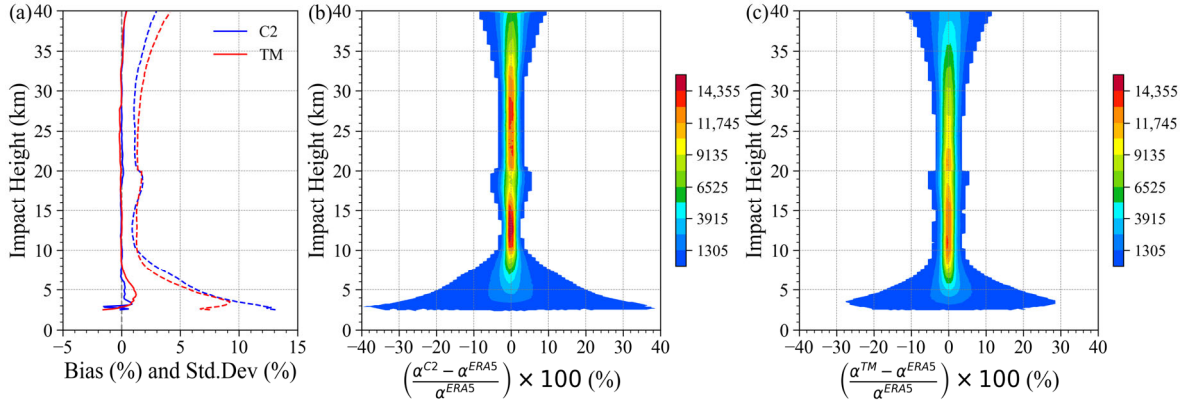


Figure 1. Vertical distributions of (**a**) the mean (%, solid lines) and standard deviation (%, dashed lines) of fractional differences in bending angle, $\left(\alpha^{GNSS} - \alpha^{ERA5}\right)/\alpha^{ERA5}$, for COSMIC-2 (blue) and Tianmu-1 (TM) RO (red) relative to ERA5 reanalysis data, and (**b**) $\left(\alpha^{COSMIC-2} - \alpha^{ERA5}\right)/\alpha^{ERA5}$ and (**c**) $\left(\alpha^{TM} - \alpha^{ERA5}\right)/\alpha^{ERA5}$ data counts within a 1% × 0.1 km box during 1–8 June 2023.

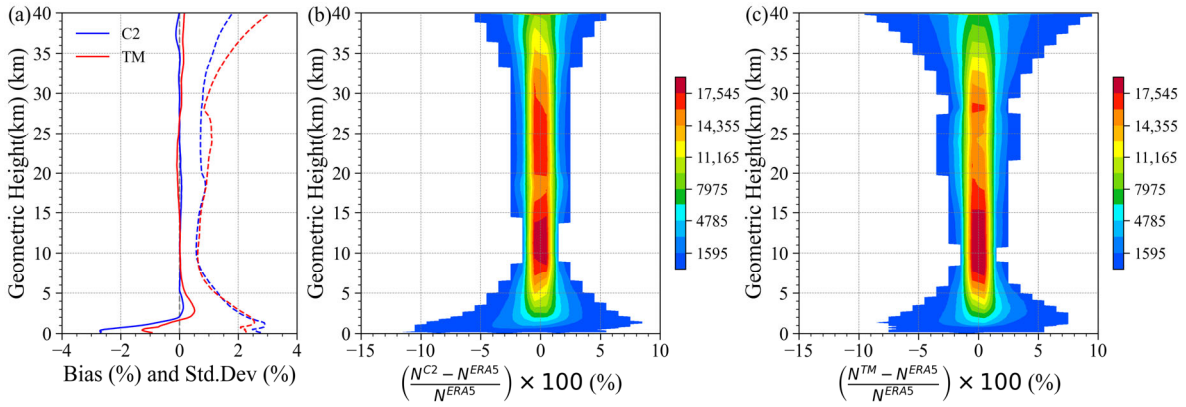


Figure 2. Vertical distributions of (**a**) the mean (%, solid lines) and standard deviation (%, dashed lines) of fractional differences in refractivity, $\left(N^{GNSS}-N^{ERA5}\right)/N^{ERA5}$, for COSMIC-2 (blue) and TM RO (red) relative to ERA5 reanalysis data, and (**b**) $\left(N^{COSMIC-2}-N^{ERA5}\right)/N^{ERA5}$ and (**c**) $\left(N^{TM}-N^{ERA5}\right)/N^{ERA5}$ data counts within a 1% × 0.1 km box during 1–8 June 2023.

Above impact and geometric heights of 30 km, the means and standard deviations of $\left(\alpha^{GNSS}-\alpha^{ERA5}\right)/\alpha^{ERA5}$ and $\left(N^{GNSS}-N^{ERA5}\right)/N^{ERA5}$ increase with height, indicating greater uncertainty in the upper-stratospheric retrievals. In the impact height range of 30–40 km, the maximum bending angle biases of COSMIC-2 and TM reach 0.39% and 0.43%, respectively. The maximum standard deviations of $\left(\alpha^{COSMIC-2}-\alpha^{ERA5}\right)/\alpha^{ERA5}$ and $\left(\alpha^{TM}-\alpha^{ERA5}\right)/\alpha^{ERA5}$ reach 2.98% and 4.14%, respectively (Figure 1a). The maximum refractivity biases (in terms of absolute value) of COSMIC-2 and TM reach values of −0.12% and 0.17%, respectively, while the maximum standard deviations of $\left(N^{COSMIC-2}-N^{ERA5}\right)/N^{ERA5}$ and $\left(N^{TM}-N^{ERA5}\right)/N^{ERA5}$ reach 1.80% and 3.06%, respectively, over the 30–40 km geometric height range (Figure 2a). The decrease in GNSS RO measurement accuracy in the upper stratosphere is caused by residual ionospheric effects [8], measurement noise [24], and initialization errors [25,26].

In the lower troposphere, GNSS radio signals are degraded by effects such as defocusing, absorption, and scattering. Consequently, the SNR decreases to the noise level, leading to large uncertainties in GNSS RO retrievals in the lower troposphere [27,28]. Figures 1 and 2 show that, below 8 km, the standard deviations of the fractional differences in bending angle and refractivity from both COSMIC-2 and TM generally increase with decreasing height. The maximum standard deviations of $\left(\alpha^{COSMIC-2}-\alpha^{ERA5}\right)/\alpha^{ERA5}$, $\left(\alpha^{TM}-\alpha^{ERA5}\right)/\alpha^{ERA5}$, $\left(N^{COSMIC-2}-N^{ERA5}\right)/N^{ERA5}$ and $\left(N^{TM}-N^{ERA5}\right)/N^{ERA5}$ are 13.11%, 9.23%, 2.91% and 2.55%, respectively. Below the impact height of 3 km/2.8 km, COSMIC-2/TM bending angle data exhibit significant negative biases relative to ERA5 reanalysis data, with minimum bias values reaching −1.53%/−1.57% (Figure 1a). Below the geometric height of 2 km/1.6 km, the COSMIC-2/TM refractivity data also exhibit significant negative biases relative to ERA5 reanalysis data, with minimum bias values reaching −2.71%/−1.27% (Figure 2a). This is mainly associated with ducting [29,30] and super-refraction [31,32]. However, both the bending angle and refractivity of TM RO exhibit positive biases in the 2.9–8 km impact height range and the 1.7–8 km geometric height range. The maximum positive biases reach 1.24% for the bending angle and 0.52% for the refractivity. This positive bias may be associated with retrieval processing differences, residual multipath effects [33,34], local spectral asymmetry [35], or representativeness errors in the moist lower troposphere. Further diagnostics are required to identify the dominant source of the bias. Because ERA5 represents gridded model fields, whereas RO retrievals represent limb sounding observations with finite horizontal sampling scales,

part of the RO–ERA5 differences, especially in the lower troposphere, may arise from representativeness and collocation errors rather than RO retrieval errors alone.

3.2. Comparison Between TM and Radiosonde

Radiosonde observations provide high vertical resolution in situ measurements and are widely used as independent reference data for validating GNSS RO retrievals [3,12]. RO–radiosonde comparisons are affected by spatial and temporal mismatch because radiosondes are point measurements, whereas RO observations represent limb sounding profiles with finite horizontal sampling scales. Figure 3 shows the spatiotemporal collocation results between COSMIC-2 and TM RO data and radiosonde observations during June–December 2023, using collocation criteria of a spatial separation of less than 200 km and a temporal difference of less than 2 h. As shown in Figure 3, the collocated radiosonde stations are broadly distributed over land areas, with clear regional differences in station density and collocated profile counts.

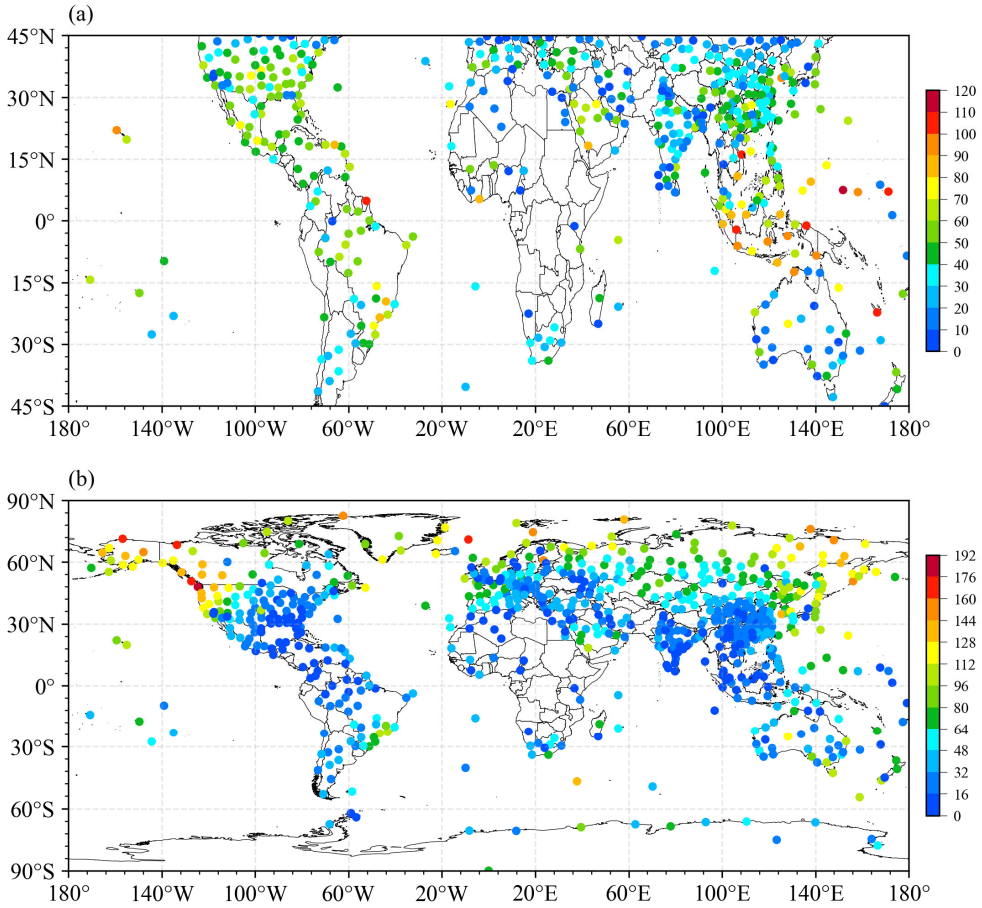


Figure 3. Spatial distribution of the numbers of (**a**) COSMIC-2 and (**b**) TM RO profiles collocated with radiosonde (RS) stations from June to December 2023.

Figures 4 and 5 show the same statistical diagnostics as Figures 1 and 2, but using radiosonde observations as the reference, for bending angle and refractivity over the period June–December 2023. Following the comparison with ERA5, analyses of $\left(\alpha^{GNSS} - \alpha^{RS}\right)/\alpha^{RS}$ and $\left(N^{GNSS} - N^{RS}\right)/N^{RS}$ are performed using similar height ranges. In the 8–25 km height range, COSMIC-2 and TM RO show comparable performance against radiosonde observations. For bending angle, the biases range from −0.37% to 0.22% (COSMIC-2) and from −0.40% to 0.21% (TM), with mean biases of −0.04% and −0.13%, respectively. The standard deviations of the fractional differences in bending angle range

from 1.51% to 4.83% for COSMIC-2 and from 1.88% to 2.74% for TM, with corresponding mean values of 2.42% and 2.24% (Figure 4a). A similar pattern is observed for refractivity, where the biases range from −0.18% to −0.01% (COSMIC-2) and from −0.21% to −0.07% (TM), with mean values of −0.08% and −0.15%, respectively. The standard deviations of the fractional differences in refractivity range from 0.54% to 1.22% and from 0.76% to 1.15%, with corresponding mean values of 0.87% and 0.99% (Figure 5a). Compared with the RO–ERA5 comparison, the RO–radiosonde standard deviations are larger, which is consistent with the stronger influence of collocation and representativeness errors in comparisons between limb sounding RO profiles and point-based radiosonde measurements.

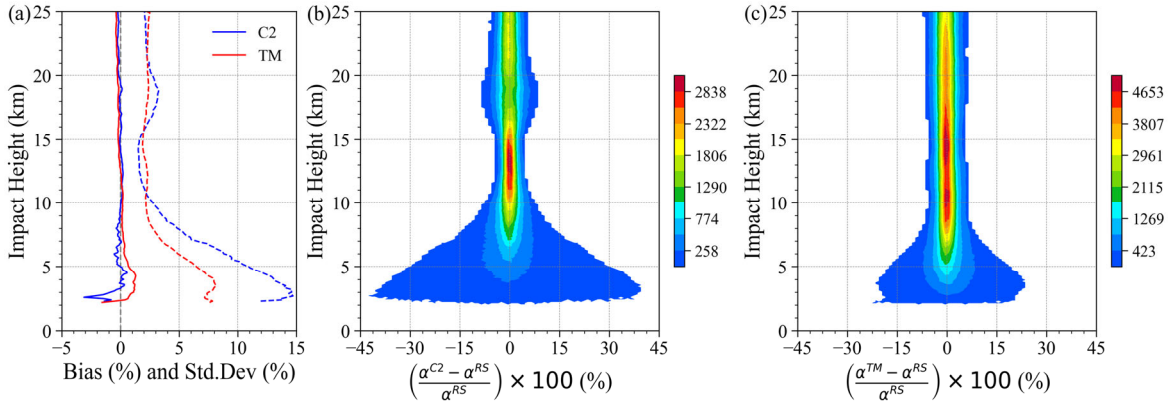


Figure 4. Vertical distributions of (**a**) the mean (%, solid lines) and standard deviation (%, dashed lines) of fractional differences in bending angle, $\left(\alpha^{GNSS}-\alpha^{RS}\right)/\alpha^{RS}$, for COSMIC-2 (blue) and TM RO (red) relative to radiosonde data, and (**b**) $\left(\alpha^{COSMIC-2}-\alpha^{RS}\right)/\alpha^{RS}$ and (**c**) $\left(\alpha^{TM}-\alpha^{RS}\right)/\alpha^{RS}$ data counts within a 1% × 0.1 km box during June–December 2023.

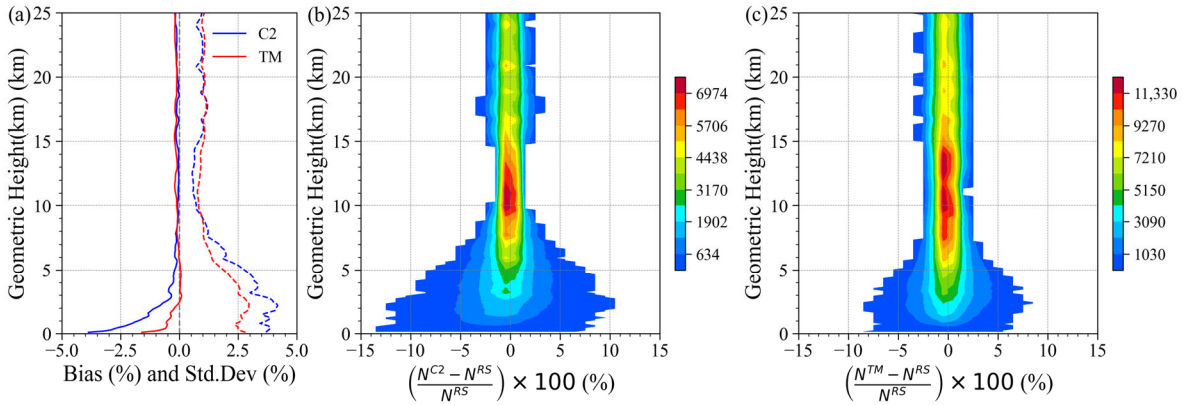


Figure 5. Vertical distributions of (**a**) the mean (%, solid lines) and standard deviation (%, dashed lines) of fractional differences in refractivity, $\left(N^{GNSS}-N^{RS}\right)/N^{RS}$, for COSMIC-2 (blue) and TM RO (red) relative to radiosonde data, and (**b**) $\left(N^{COSMIC-2}-N^{RS}\right)/N^{RS}$ and (**c**) $\left(N^{TM}-N^{RS}\right)/N^{RS}$ data counts within a 1% × 0.1 km box during June–December 2023.

Below an impact height of 3.2 km, COSMIC-2 exhibits negative bending angle biases relative to radiosonde observations, with a minimum bias of −3.12%. In contrast, TM RO exhibits positive bending angle biases between 2.4 and 8 km, with a maximum of 1.30%, whereas negative biases occur below 2.4 km, reaching −1.57% (Figure 4a). Below the geometric height of 8 km/2.4 km, the COSMIC-2/TM refractivity data exhibit significant negative biases relative to radiosonde observations, with minimum negative biases reaching −3.87%/−1.60%. Unlike COSMIC-2, TM refractivity exhibits a weak positive bias between geometric heights of 2.5–6 km, with a maximum of 0.10%. The larger differences between TM and radiosonde observations are larger below 8 km than at higher heights.

3.3. Comparison Between TM and COSMIC-2

Because comparisons with ERA5 and radiosonde data may include model-related, forward operator, and representativeness errors, COSMIC-2 RO data are further used as a peer RO dataset for consistency evaluation, rather than as an absolute reference. Compared with model and radiosonde references, the TM–COSMIC-2 comparison reduces part of the inconsistency caused by differences in observation geometry and retrieval variables. However, COSMIC-2 should not be regarded as an absolute truth, and the comparison is also influenced by sampling differences and collocation uncertainty. The collocation criteria between TM and COSMIC-2 RO profiles are a temporal difference of less than 30 min and a spatial distance of less than 50 km from June to December 2023. To reduce uncertainties associated with spatiotemporal collocation, the collocated data are divided into two groups according to the angle between the occultation planes: $\leq$45° (corresponding to azimuth angle differences of 0–45° and 135–180°) and >45° (corresponding to azimuth angle differences of 45–90° and 90–135°). Figure 6 presents the spatial distributions of the collocated TM and COSMIC-2 data for the two groups. The collocated samples are distributed uniformly in both groups, indicating that the azimuth angle classification does not introduce noticeable spatial sampling biases.

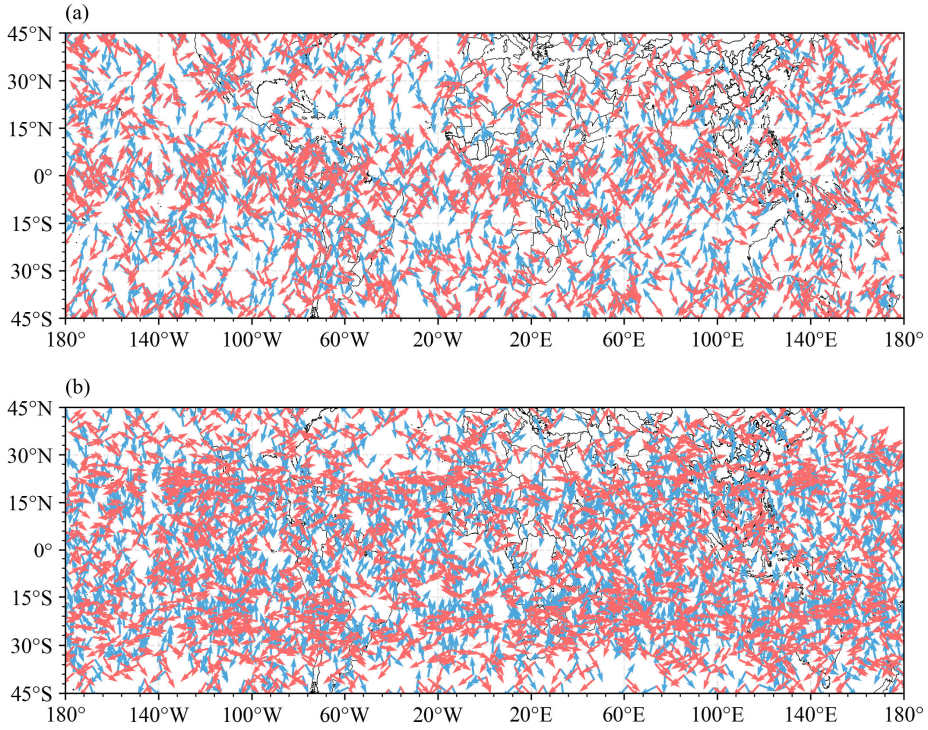


Figure 6. Spatial distributions of collocated COSMIC-2 (blue) and TM (red) RO profiles with azimuth angle differences of (**a**) 0–45° and 135–180° and (**b**) 45–90° and 90–135° during June–December 2023. The 400 km length arrows indicate the ray direction at the perigee.

Figures 7 and 8 show comparisons of retrieved bending angle and refractivity between COSMIC-2 RO and TM RO, together with the corresponding data counts, from June to December 2023. The results show that when the azimuth angle differences are within the ranges of 0–45° and 135–180°, the fractional differences in bending angle between TM and COSMIC-2 RO data are smaller than those observed for azimuth angle differences of 45–90° and 90–135°. The maximum bias decreases from 2.24% to 1.86%, while the standard deviation decreases from 12.62% to 12.14% (Figure 7). A similar behavior is observed for refractivity, with the maximum bias decreasing from 0.95% to 0.71% and the standard deviation decreasing from 3.07% to 2.93% (Figure 8). These results indicate

that the direction of the occultation rays should also be considered when performing the collocation of RO profiles, in addition to conventional spatial and temporal constraints. In the following analysis, a detailed comparison between TM and COSMIC-2 is presented for cases with azimuth angle differences of 0–45° and 135–180°.

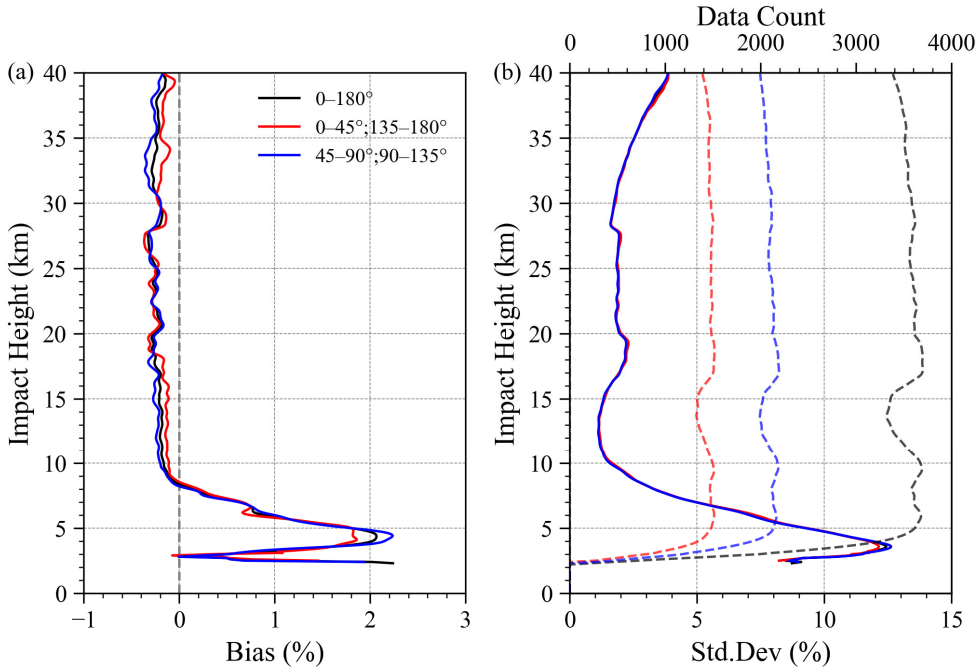


Figure 7. Vertical distributions of (**a**) the mean (%) and (**b**) standard deviation (%, solid lines) and data counts (dashed lines) of fractional differences in bending angle, $\left(\alpha^{TM} - \alpha^{COSMIC-2}\right)/\alpha^{COSMIC-2}$, for collocated TM and COSMIC-2 RO profiles with azimuth angle differences of 0–45° and 135–180° (red), 45–90° and 90–135° (blue), and 0–180° (black) during June–December 2023.

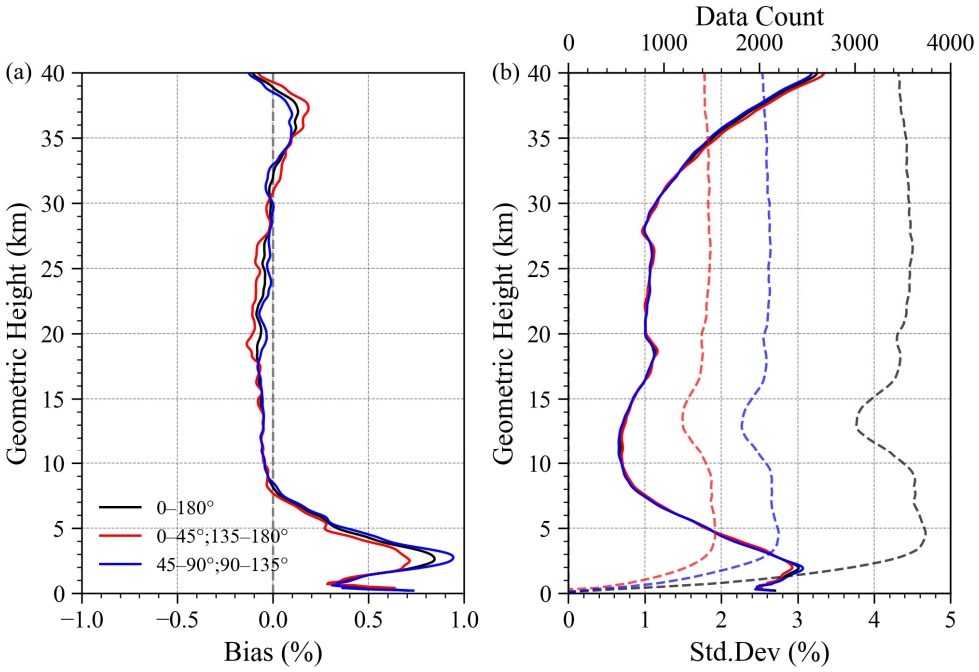


Figure 8. Vertical distributions of (**a**) the mean (%) and (**b**) standard deviation (%, solid lines) and data counts (dashed lines) of fractional differences in refractivity, $\left(N^{TM} - N^{COSMIC-2}\right)/N^{COSMIC-2}$, for collocated TM and COSMIC-2 RO profiles with azimuth angle differences of 0–45° and 135–180° (red), 45–90° and 90–135° (blue), and 0–180° (black) during June–December 2023.

Within the 8–30 km impact/geometric height range, the bending angle bias of TM relative to COSMIC-2 ranges from −0.37% to 0.20%, with a mean value of −0.20%, while the refractivity bias ranges from −0.14% to −0.02%, with an average value of −0.07%. The corresponding standard deviations of $\left(\alpha^{TM} - \alpha^{COSMIC-2}\right)/\alpha^{COSMIC-2}$ and $\left(N^{TM} - N^{COSMIC-2}\right)/N^{COSMIC-2}$ vary between 1.15% and 3.32% and between 0.70% and 1.17%, respectively, with corresponding mean values of 1.80% and 0.95% (Figures 7 and 8). These results indicate that TM and COSMIC-2 have broadly consistent bending angle and refractivity retrievals in the upper troposphere and lower stratosphere.

Above the impact/geometric height of 30 km, the maximum bending angle/refractivity biases (in terms of absolute value) of TM relative to COSMIC-2 reach −0.24% and 0.16%, respectively. The maximum standard deviations of $\left(\alpha^{TM} - \alpha^{COSMIC-2}\right)/\alpha^{COSMIC-2}$ and $\left(N^{TM} - N^{COSMIC-2}\right)/N^{COSMIC-2}$ reach 3.87% and 3.35%, respectively (Figures 6 and 7). In contrast to the negative bending angle and refractivity biases found between 8 and 30 km, positive biases occur in the lower troposphere (0–8 km), suggesting that TM measurements are generally higher than those from COSMIC-2 at these heights. The maximum positive biases of bending angle and refractivity reach 1.86% and 0.71%, respectively. The maximum standard deviations of $\left(\alpha^{TM} - \alpha^{COSMIC-2}\right)/\alpha^{COSMIC-2}$ and $\left(N^{TM} - N^{COSMIC-2}\right)/N^{COSMIC-2}$ reach 12.14% and 2.93%, respectively. Compared with the 8–40 km height range, larger differences between TM and COSMIC-2 are observed for both bending angle and refractivity in the lower troposphere.

3.4. Observation Error Estimates

Figures 9 and 10 show the normalized observation errors of bending angle and refractivity for COSMIC-2 and TM RO, respectively, estimated using the 3CH method. As shown in Figure 9, within the impact height range of 3–12 km, the bending angle observation errors for both COSMIC-2 and TM RO decrease with height, consistent with the increasing observational uncertainty of GNSS RO measurements at lower heights [36]. The three error estimates are in good agreement across all height levels. Their differences are slightly larger below the impact height of 8 km than above. At impact heights of 2.9 km for COSMIC-2 and 3.5 km for TM RO, the 3CH-estimated bending angle observation errors reach their maximum values of 12.50% and 8.54%, respectively. Below an impact height of 10 km, the estimated bending angle errors for TM RO are smaller than those for COSMIC-2 RO. This difference should be interpreted cautiously because the 3CH-derived estimates represent effective observation errors for the collocated samples rather than instrument-only measurement errors. They may be affected by sampling differences, lower tropospheric penetration depth, representativeness errors, collocation errors, and residual error correlations among the reference datasets. Smaller TM estimates below 10 km do not necessarily indicate better intrinsic lower tropospheric performance than those of COSMIC-2. In the impact height range of 10–15 km, the bending angle observation error estimates for both datasets reach their minimum values, remaining at approximately 1%.

The refractivity observation errors shown in Figure 10 exhibit characteristics similar to those of the bending angle observation errors. Refractivity observation errors decrease with geometric height over the 2–12 km range for both COSMIC-2 and TM RO. The three error estimates are in good agreement across all height levels, with the closest agreement occurring between 8 and 15 km. Within this height range, the refractivity observation error of COSMIC-2 RO remains at approximately 0.5%, whereas that of TM RO is around 1%. The refractivity observation errors for both COSMIC-2 and TM RO are larger below the geometric height of 8 km. At geometric heights of 1.1 km for COSMIC-2 and 2.1 km for TM RO, the refractivity observation errors reach their maximum values of 2.70% and 2.42%, respectively.

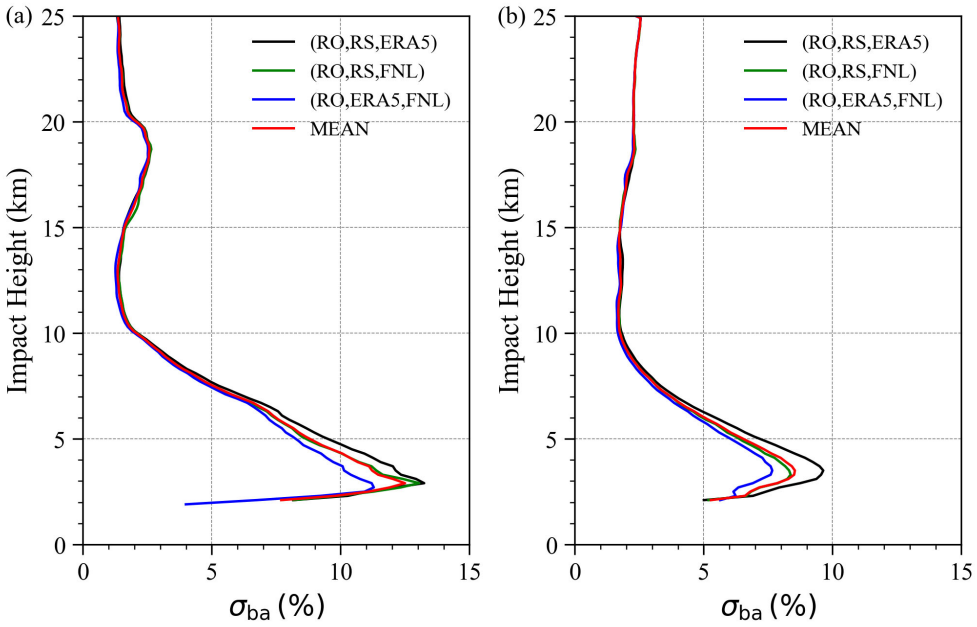


Figure 9. Vertical distributions of the three estimated observation errors (σ_1, black solid line; σ_2, green solid line; and σ_3, blue solid line) and their mean (red solid line) for (**a**) COSMIC-2 RO and (**b**) TM RO bending angles, calculated using data from June to December 2023.

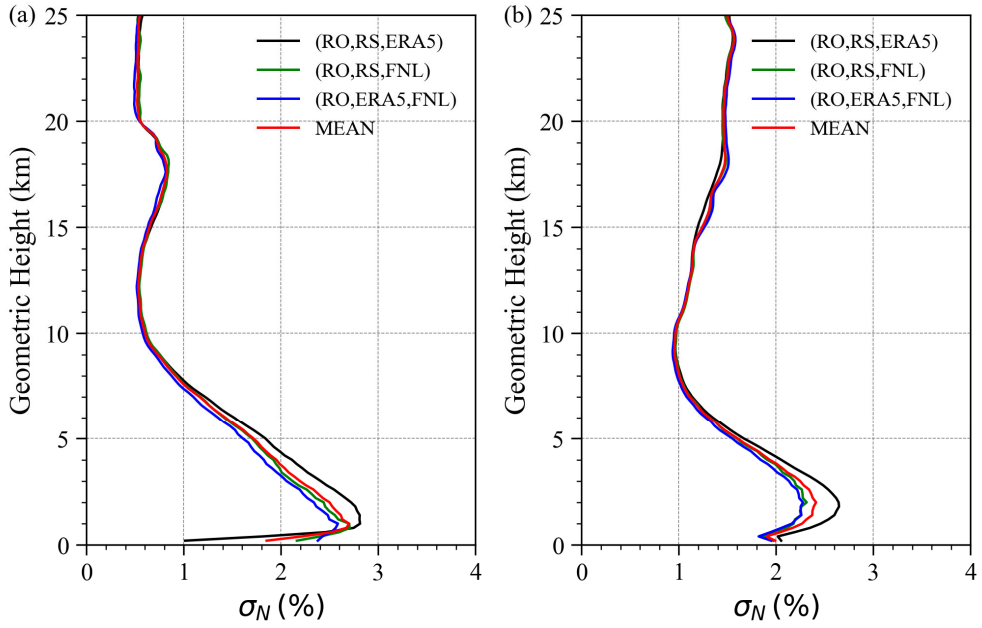


Figure 10. Vertical distributions of the three estimated observation errors (σ_1, black solid line; σ_2, green solid line; and σ_3, blue solid line) and their mean (red solid line) for (**a**) COSMIC-2 RO and (**b**) TM RO refractivity, calculated using data from June to December 2023.

In actual assimilation systems, unnormalized observation errors are used. Therefore, we present the meridional vertical cross sections of the unnormalized observation errors for the COSMIC-2 and TM bending angle and refractivity data in Figure 11. For both bending angle and refractivity, the observation errors of COSMIC-2 and TM are larger in the tropics ($\pm 30^\circ$ latitude) and smaller in the middle and high latitudes, showing a clear latitudinal dependence. Below 4 km, the observation errors in bending angle and refractivity for COSMIC-2 and TM reach their maximum values near 10°S in the Southern Hemisphere and 20°N in the Northern Hemisphere. The larger errors over parts of the tropical Southern

Hemisphere may be associated with stronger lower-tropospheric moisture variability and the more extensive oceanic coverage in this region. Tables 1 and 2 list the specific values of the observation errors for TM RO bending angle and refractivity, respectively. These values are averaged within each 10° latitudinal band from 60°S to 60°N over the impact height range of 2.1–11.1 km and the geometric height range of 0.1–9.1 km. The value 999. in Table 1 is a flag value indicating that no valid observation error estimate is available for that location.

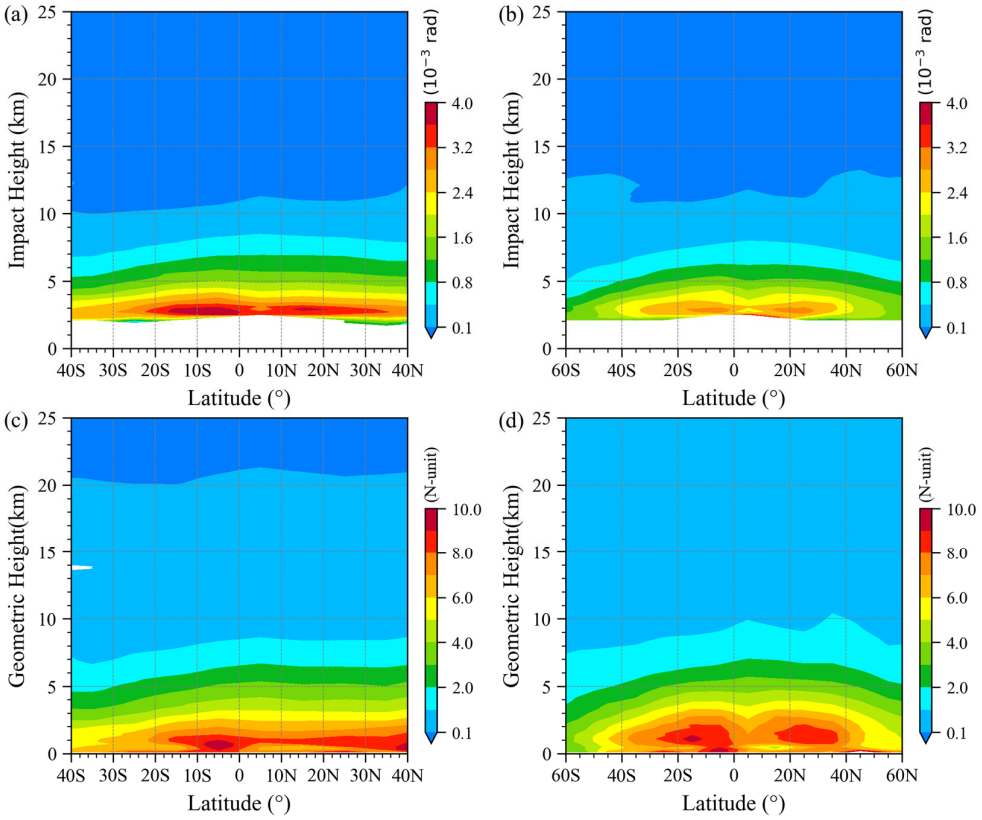


Figure 11. Meridional vertical cross sections of the unnormalized observation errors for (**a**,**b**) bending angle and (**c**,**d**) refractivity of COSMIC-2 (**left**) and TM (**right**) within a 5° × 0.2 km box from June to December 2023.

Table 1. Mean observation errors (unit: 10^{-3} rad) of TM RO bending angle between the impact heights of 2.1–25.1 km, averaged within each 10° latitudinal band from 60°S to 60°N.

IH (km)\°	60–50°S	50–40°S	40–30°S	30–20°S	20–10°S	10°S–0°	0–10°N	10–20°N	20–30°N	30–40°N	40–50°N	50–60°N
2.1	1.25	1.33	1.17	1.26	999.	999.	999.	999.	1.21	0.87	1.38	1.37
2.3	1.46	1.69	1.99	1.71	1.89	999.	999.	3.39	2.10	1.70	1.71	1.54
2.5	1.38	1.69	2.34	2.47	2.43	2.10	3.45	2.41	2.72	2.05	1.82	1.57
2.7	1.30	1.78	2.33	2.71	2.76	3.10	1.72	2.75	2.98	2.38	1.84	1.58
2.9	1.28	1.88	2.37	2.56	2.85	3.10	2.26	2.87	2.93	2.53	1.84	1.55
3.1	1.32	1.84	2.34	2.50	2.55	2.64	2.45	2.67	2.73	2.52	1.81	1.56
3.3	1.13	1.66	2.28	2.43	2.49	2.44	2.10	2.37	2.56	2.42	1.76	1.53
3.5	1.01	1.52	2.05	2.28	2.44	2.36	2.03	2.24	2.40	2.24	1.73	1.46
3.7	0.89	1.37	1.80	2.06	2.29	2.37	1.94	2.17	2.27	2.09	1.65	1.37
3.9	0.81	1.25	1.56	1.89	2.20	2.22	1.82	2.09	2.09	1.92	1.54	1.30
4.1	0.72	1.14	1.44	1.74	2.01	2.10	1.76	1.97	1.93	1.75	1.44	1.21
4.3	0.70	0.96	1.27	1.54	1.79	2.02	1.59	1.83	1.77	1.58	1.33	1.10
4.5	0.65	0.86	1.19	1.41	1.67	1.78	1.50	1.66	1.60	1.45	1.22	1.03

Table 1. *Cont.*

IH (km)\°	60–50° S	50–40° S	40–30° S	30–20° S	20–10° S	10° S–0°	0–10° N	10–20° N	20–30° N	30–40° N	40–50° N	50–60° N
4.7	0.54	0.78	1.11	1.32	1.51	1.59	1.38	1.49	1.44	1.34	1.13	0.95
4.9	0.47	0.74	0.97	1.19	1.39	1.45	1.28	1.34	1.33	1.21	1.05	0.86
5.1	0.45	0.68	0.86	1.10	1.23	1.35	1.14	1.23	1.21	1.13	0.97	0.79
5.3	0.44	0.62	0.77	1.00	1.15	1.23	1.09	1.11	1.12	1.00	0.89	0.72
5.5	0.42	0.58	0.70	0.92	1.07	1.10	1.01	1.01	1.05	0.94	0.83	0.66
5.7	0.39	0.51	0.63	0.86	1.00	1.03	0.95	0.93	0.96	0.87	0.77	0.61
5.9	0.37	0.47	0.57	0.77	0.88	0.93	0.89	0.87	0.87	0.80	0.70	0.55
6.1	0.34	0.42	0.53	0.70	0.80	0.85	0.82	0.84	0.81	0.73	0.63	0.50
6.3	0.30	0.37	0.48	0.64	0.75	0.79	0.76	0.77	0.76	0.67	0.57	0.46
6.5	0.28	0.33	0.44	0.57	0.67	0.71	0.71	0.69	0.69	0.61	0.52	0.42
6.7	0.25	0.30	0.41	0.50	0.59	0.65	0.67	0.64	0.63	0.55	0.47	0.38
6.9	0.23	0.29	0.38	0.46	0.54	0.58	0.62	0.60	0.58	0.50	0.43	0.34
7.1	0.22	0.26	0.34	0.42	0.50	0.54	0.55	0.55	0.52	0.46	0.39	0.31
7.3	0.20	0.24	0.30	0.38	0.44	0.48	0.52	0.51	0.47	0.42	0.35	0.28
7.5	0.20	0.22	0.28	0.34	0.40	0.44	0.47	0.47	0.44	0.39	0.32	0.26
7.7	0.19	0.20	0.25	0.32	0.36	0.41	0.44	0.44	0.41	0.35	0.29	0.24
7.9	0.17	0.18	0.23	0.29	0.34	0.38	0.41	0.40	0.37	0.33	0.27	0.22
8.1	0.15	0.17	0.20	0.26	0.30	0.34	0.38	0.37	0.33	0.30	0.24	0.20
8.3	0.15	0.16	0.19	0.23	0.27	0.31	0.35	0.34	0.30	0.28	0.22	0.18
8.5	0.15	0.15	0.18	0.21	0.26	0.28	0.32	0.31	0.28	0.25	0.20	0.17
8.7	0.14	0.14	0.16	0.20	0.24	0.26	0.29	0.28	0.26	0.23	0.19	0.16
8.9	0.13	0.13	0.15	0.18	0.21	0.24	0.27	0.26	0.24	0.21	0.17	0.15
9.1	0.12	0.12	0.14	0.17	0.19	0.22	0.25	0.23	0.22	0.20	0.16	0.14
9.3	0.11	0.12	0.13	0.15	0.17	0.20	0.23	0.22	0.20	0.18	0.15	0.13
9.5	0.11	0.12	0.13	0.14	0.16	0.19	0.21	0.20	0.18	0.17	0.14	0.12
9.7	0.12	0.11	0.12	0.14	0.15	0.17	0.19	0.18	0.17	0.16	0.13	0.12
9.9	0.13	0.11	0.11	0.13	0.14	0.16	0.17	0.16	0.15	0.15	0.13	0.12
10.1	0.13	0.11	0.11	0.12	0.13	0.15	0.16	0.15	0.14	0.15	0.12	0.11
10.3	0.12	0.11	0.11	0.11	0.12	0.13	0.15	0.14	0.13	0.14	0.12	0.11
10.5	0.12	0.11	0.10	0.11	0.11	0.12	0.14	0.13	0.12	0.13	0.12	0.11
10.7	0.12	0.11	0.10	0.10	0.11	0.12	0.13	0.12	0.12	0.13	0.12	0.11
10.9	0.12	0.11	0.10	0.10	0.10	0.11	0.12	0.11	0.11	0.12	0.11	0.11
11.1	0.13	0.12	0.10	0.10	0.09	0.10	0.11	0.11	0.10	0.12	0.11	0.11
11.3	0.12	0.12	0.10	0.09	0.09	0.10	0.11	0.10	0.10	0.11	0.11	0.11
11.5	0.12	0.11	0.10	0.09	0.09	0.09	0.10	0.10	0.09	0.11	0.11	0.11
11.7	0.13	0.12	0.10	0.09	0.09	0.09	0.10	0.09	0.09	0.11	0.11	0.11
11.9	0.13	0.12	0.10	0.09	0.08	0.09	0.10	0.09	0.09	0.11	0.11	0.11
12.1	0.12	0.12	0.10	0.09	0.08	0.08	0.09	0.09	0.08	0.11	0.11	0.11
12.3	0.12	0.11	0.10	0.09	0.08	0.08	0.09	0.08	0.08	0.11	0.11	0.11
12.5	0.11	0.11	0.10	0.09	0.08	0.08	0.08	0.08	0.08	0.10	0.11	0.10
12.7	0.10	0.11	0.09	0.08	0.08	0.08	0.08	0.08	0.08	0.10	0.11	0.10
12.9	0.09	0.10	0.09	0.08	0.08	0.08	0.08	0.08	0.07	0.10	0.10	0.09
13.1	0.09	0.09	0.09	0.08	0.07	0.08	0.08	0.07	0.07	0.10	0.10	0.09
13.3	0.09	0.09	0.09	0.08	0.07	0.07	0.08	0.07	0.07	0.09	0.10	0.09
13.5	0.09	0.09	0.09	0.08	0.07	0.07	0.07	0.07	0.07	0.09	0.10	0.08
13.7	0.08	0.08	0.08	0.07	0.07	0.07	0.07	0.07	0.07	0.09	0.09	0.08
13.9	0.08	0.08	0.08	0.07	0.07	0.07	0.07	0.07	0.07	0.09	0.09	0.08
14.1	0.08	0.07	0.08	0.07	0.06	0.06	0.07	0.07	0.07	0.09	0.09	0.07
14.3	0.08	0.07	0.07	0.07	0.06	0.06	0.07	0.07	0.07	0.08	0.08	0.07
14.5	0.07	0.07	0.07	0.07	0.06	0.07	0.07	0.07	0.06	0.08	0.08	0.07
14.7	0.07	0.07	0.07	0.07	0.06	0.07	0.07	0.06	0.06	0.08	0.08	0.07

Table 1. *Cont.*

IH (km)\°	60–50° S	50–40° S	40–30° S	30–20° S	20–10° S	10° S–0°	0–10° N	10–20° N	20–30° N	30–40° N	40–50° N	50–60° N
14.9	0.07	0.07	0.07	0.07	0.06	0.06	0.07	0.06	0.06	0.08	0.08	0.06
15.1	0.07	0.07	0.07	0.07	0.06	0.07	0.07	0.06	0.06	0.08	0.07	0.06
15.3	0.06	0.07	0.06	0.07	0.06	0.07	0.07	0.06	0.06	0.07	0.07	0.06
15.5	0.07	0.07	0.06	0.07	0.06	0.07	0.08	0.07	0.06	0.07	0.07	0.06
15.7	0.07	0.06	0.07	0.06	0.06	0.07	0.08	0.07	0.06	0.07	0.07	0.06
15.9	0.06	0.06	0.06	0.06	0.06	0.07	0.08	0.07	0.06	0.07	0.07	0.06
16.1	0.06	0.06	0.06	0.06	0.06	0.07	0.08	0.07	0.06	0.07	0.07	0.06
16.3	0.06	0.06	0.06	0.06	0.06	0.07	0.08	0.07	0.06	0.07	0.07	0.06
16.5	0.06	0.06	0.06	0.06	0.06	0.07	0.08	0.07	0.06	0.07	0.06	0.05
16.7	0.06	0.06	0.06	0.06	0.06	0.07	0.08	0.07	0.06	0.07	0.06	0.05
16.9	0.05	0.05	0.06	0.06	0.06	0.07	0.08	0.07	0.06	0.07	0.06	0.05
17.1	0.05	0.05	0.06	0.06	0.06	0.06	0.08	0.07	0.06	0.06	0.06	0.05
17.3	0.05	0.05	0.06	0.06	0.06	0.06	0.08	0.07	0.06	0.06	0.06	0.05
17.5	0.05	0.05	0.06	0.06	0.06	0.06	0.07	0.07	0.06	0.06	0.05	0.05
17.7	0.05	0.05	0.06	0.06	0.06	0.06	0.07	0.07	0.06	0.06	0.05	0.04
17.9	0.05	0.05	0.05	0.06	0.06	0.06	0.07	0.07	0.06	0.06	0.05	0.04
18.1	0.05	0.05	0.05	0.06	0.06	0.06	0.07	0.07	0.06	0.06	0.05	0.04
18.3	0.05	0.04	0.05	0.06	0.06	0.06	0.07	0.07	0.06	0.06	0.05	0.04
18.5	0.05	0.04	0.05	0.06	0.06	0.06	0.07	0.07	0.06	0.06	0.05	0.04
18.7	0.04	0.04	0.05	0.06	0.06	0.06	0.07	0.07	0.05	0.06	0.05	0.04
18.9	0.04	0.04	0.05	0.05	0.05	0.06	0.06	0.06	0.05	0.05	0.05	0.04
19.1	0.04	0.04	0.05	0.05	0.05	0.05	0.06	0.06	0.05	0.05	0.04	0.04
19.3	0.04	0.04	0.04	0.05	0.05	0.05	0.05	0.05	0.05	0.05	0.04	0.04
19.5	0.04	0.04	0.04	0.05	0.05	0.05	0.05	0.05	0.05	0.05	0.04	0.03
19.7	0.04	0.04	0.04	0.04	0.05	0.05	0.05	0.05	0.04	0.05	0.04	0.03
19.9	0.03	0.04	0.04	0.04	0.04	0.04	0.05	0.05	0.04	0.04	0.04	0.03
20.1	0.03	0.04	0.04	0.04	0.04	0.04	0.05	0.05	0.04	0.04	0.04	0.03
20.3	0.04	0.04	0.04	0.04	0.04	0.04	0.04	0.05	0.04	0.04	0.04	0.03
20.5	0.04	0.03	0.04	0.04	0.04	0.04	0.04	0.04	0.04	0.04	0.03	0.03
20.7	0.04	0.03	0.03	0.04	0.04	0.04	0.04	0.04	0.04	0.04	0.03	0.03
20.9	0.03	0.03	0.03	0.03	0.03	0.04	0.04	0.04	0.03	0.04	0.03	0.03
21.1	0.03	0.03	0.03	0.03	0.03	0.04	0.04	0.04	0.03	0.04	0.03	0.03
21.3	0.03	0.03	0.03	0.03	0.03	0.03	0.04	0.03	0.03	0.03	0.03	0.03
21.5	0.03	0.03	0.03	0.03	0.03	0.03	0.04	0.03	0.03	0.03	0.03	0.03
21.7	0.03	0.03	0.03	0.03	0.03	0.03	0.03	0.03	0.03	0.03	0.03	0.03
21.9	0.03	0.03	0.03	0.03	0.03	0.03	0.03	0.03	0.03	0.03	0.03	0.03
22.1	0.03	0.03	0.03	0.03	0.03	0.03	0.03	0.03	0.03	0.03	0.03	0.02
22.3	0.03	0.03	0.03	0.03	0.03	0.03	0.03	0.03	0.03	0.03	0.03	0.02
22.5	0.03	0.03	0.03	0.03	0.03	0.03	0.03	0.03	0.02	0.03	0.03	0.02
22.7	0.03	0.03	0.02	0.02	0.03	0.03	0.03	0.03	0.02	0.03	0.03	0.02
22.9	0.03	0.02	0.02	0.02	0.02	0.02	0.03	0.03	0.02	0.03	0.02	0.02
23.1	0.03	0.02	0.02	0.02	0.02	0.02	0.03	0.03	0.02	0.03	0.02	0.02
23.3	0.03	0.02	0.02	0.02	0.02	0.02	0.03	0.02	0.02	0.02	0.02	0.02
23.5	0.02	0.02	0.02	0.02	0.02	0.02	0.02	0.02	0.02	0.02	0.02	0.02
23.7	0.02	0.02	0.02	0.02	0.02	0.02	0.02	0.02	0.02	0.02	0.02	0.02
23.9	0.02	0.02	0.02	0.02	0.02	0.02	0.02	0.02	0.02	0.02	0.02	0.02
24.1	0.02	0.02	0.02	0.02	0.02	0.02	0.02	0.02	0.02	0.02	0.02	0.02
24.3	0.02	0.02	0.02	0.02	0.02	0.02	0.02	0.02	0.02	0.02	0.02	0.02
24.5	0.02	0.02	0.02	0.02	0.02	0.02	0.02	0.02	0.02	0.02	0.02	0.02
24.7	0.02	0.02	0.02	0.02	0.02	0.02	0.02	0.02	0.02	0.02	0.02	0.02

Table 1. *Cont.*

IH (km)\°	60–50°S	50–40°S	40–30°S	30–20°S	20–10°S	10°S–0°	0–10°N	10–20°N	20–30°N	30–40°N	40–50°N	50–60°N
24.9	0.02	0.02	0.02	0.02	0.02	0.02	0.02	0.02	0.02	0.02	0.02	0.02
25.1	0.02	0.02	0.01	0.01	0.02	0.02	0.02	0.02	0.01	0.02	0.02	0.01

Table 2. Mean observation errors (N-unit) of TM RO refractivity between the geometric heights of 0.1–25.1 km, averaged within each 10° latitudinal band from 60°S to 60°N.

GH (km)\°	60–50°S	50–40°S	40–30°S	30–20°S	20–10°S	10°S–0°	0–10°N	10–20°N	20–30°N	30–40°N	40–50°N	50–60°N
0.1	2.83	6.30	6.98	9.10	7.48	10.0	6.67	7.95	7.73	6.55	12.36	8.09
0.3	3.60	5.64	6.30	6.93	7.00	9.76	7.09	5.12	7.10	7.19	7.12	5.56
0.5	3.66	5.32	6.50	7.06	6.78	8.72	5.79	4.50	6.62	7.34	6.09	5.18
0.7	3.96	5.53	7.06	7.63	8.30	8.93	6.96	6.77	7.89	8.00	5.98	5.29
0.9	4.22	5.80	7.25	7.95	9.13	8.36	7.51	7.60	8.72	8.48	6.09	5.39
1.1	4.18	5.98	7.42	8.23	9.35	8.41	7.26	7.93	8.94	8.51	6.13	5.32
1.3	4.27	5.73	7.38	7.95	9.08	8.40	7.06	7.91	8.76	8.44	6.14	5.20
1.5	4.10	5.48	7.13	7.95	8.77	8.52	6.95	8.09	8.64	8.38	6.19	5.16
1.7	3.76	5.15	6.71	7.73	8.37	8.41	6.85	7.86	8.35	8.02	6.09	5.03
1.9	3.60	5.02	6.21	7.38	8.02	8.19	6.69	7.76	8.23	7.70	6.02	4.90
2.1	3.46	4.83	5.88	7.15	8.10	8.03	6.53	7.72	8.12	7.43	5.92	4.78
2.3	3.31	4.60	5.50	6.62	7.66	7.70	6.26	7.40	7.67	7.12	5.71	4.64
2.5	3.09	4.30	5.25	6.36	7.43	7.39	6.00	7.24	7.34	6.75	5.52	4.49
2.7	2.93	3.87	4.95	6.07	7.14	7.21	5.83	7.11	6.96	6.45	5.32	4.30
2.9	2.80	3.65	4.62	5.78	6.58	6.68	5.62	6.73	6.49	6.07	5.08	4.13
3.1	2.60	3.53	4.40	5.50	6.23	6.31	5.51	6.35	6.17	5.77	4.87	3.97
3.3	2.37	3.32	4.11	5.15	5.98	5.94	5.29	5.92	5.86	5.49	4.66	3.76
3.5	2.25	3.19	3.77	4.80	5.53	5.44	4.97	5.54	5.51	5.18	4.40	3.55
3.7	2.20	3.01	3.50	4.55	5.18	5.18	4.74	5.28	5.24	4.92	4.19	3.39
3.9	2.13	2.77	3.26	4.29	4.91	4.95	4.51	4.99	5.00	4.65	3.98	3.19
4.1	2.09	2.56	3.03	4.02	4.56	4.56	4.26	4.65	4.72	4.36	3.77	2.98
4.3	1.97	2.42	2.86	3.83	4.29	4.28	4.10	4.42	4.45	4.12	3.57	2.82
4.5	1.86	2.27	2.67	3.64	4.10	4.11	3.97	4.23	4.19	3.91	3.39	2.64
4.7	1.76	2.15	2.50	3.35	3.79	3.90	3.85	4.02	3.88	3.65	3.19	2.47
4.9	1.67	1.99	2.35	3.09	3.45	3.63	3.71	3.81	3.61	3.43	2.99	2.31
5.1	1.58	1.85	2.25	2.88	3.18	3.41	3.57	3.55	3.39	3.23	2.82	2.17
5.3	1.50	1.72	2.13	2.64	3.01	3.19	3.38	3.31	3.18	3.03	2.64	2.03
5.5	1.43	1.60	2.00	2.41	2.78	2.88	3.16	3.08	2.96	2.82	2.48	1.90
5.7	1.38	1.51	1.91	2.23	2.56	2.70	2.99	2.86	2.78	2.68	2.34	1.78
5.9	1.36	1.44	1.79	2.12	2.41	2.59	2.80	2.71	2.61	2.55	2.20	1.67
6.1	1.34	1.38	1.66	1.93	2.22	2.40	2.59	2.56	2.43	2.40	2.04	1.57
6.3	1.33	1.32	1.55	1.78	2.05	2.18	2.41	2.41	2.25	2.25	1.91	1.48
6.5	1.31	1.26	1.46	1.71	1.90	2.04	2.28	2.26	2.11	2.11	1.80	1.40
6.7	1.27	1.21	1.38	1.64	1.83	1.95	2.19	2.13	1.98	1.99	1.70	1.33
6.9	1.21	1.16	1.29	1.53	1.70	1.85	2.06	2.02	1.86	1.87	1.61	1.26
7.1	1.14	1.12	1.22	1.43	1.57	1.70	1.96	1.88	1.73	1.76	1.51	1.19
7.3	1.08	1.08	1.15	1.37	1.47	1.57	1.83	1.78	1.63	1.68	1.44	1.14
7.5	1.04	1.05	1.11	1.29	1.40	1.47	1.71	1.66	1.54	1.60	1.37	1.09
7.7	0.99	1.02	1.07	1.22	1.36	1.40	1.61	1.56	1.46	1.54	1.31	1.05
7.9	0.97	0.99	1.03	1.16	1.28	1.33	1.52	1.46	1.37	1.47	1.26	1.01
8.1	0.95	0.97	0.99	1.11	1.20	1.27	1.46	1.37	1.31	1.40	1.21	0.99
8.3	0.94	0.95	0.96	1.06	1.13	1.20	1.40	1.30	1.24	1.35	1.16	0.96

Table 2. *Cont.*

GH (km)\°	60–50° S	50–40° S	40–30° S	30–20° S	20–10° S	10° S–0°	0–10° N	10–20° N	20–30° N	30–40° N	40–50° N	50–60° N
8.5	0.94	0.94	0.94	1.02	1.08	1.15	1.32	1.24	1.18	1.30	1.13	0.94
8.7	0.93	0.91	0.92	0.99	1.02	1.10	1.25	1.18	1.11	1.25	1.09	0.92
8.9	0.92	0.90	0.89	0.95	0.96	1.04	1.20	1.12	1.05	1.21	1.06	0.90
9.1	0.91	0.89	0.88	0.93	0.91	0.99	1.15	1.07	0.98	1.17	1.03	0.88
9.3	0.86	0.89	0.85	0.90	0.87	0.95	1.11	1.02	0.93	1.15	1.01	0.87
9.5	0.85	0.87	0.84	0.87	0.84	0.93	1.06	0.98	0.89	1.12	0.99	0.86
9.7	0.86	0.87	0.83	0.85	0.81	0.91	1.03	0.94	0.86	1.09	0.98	0.85
9.9	0.88	0.86	0.82	0.82	0.80	0.87	1.00	0.90	0.83	1.06	0.97	0.84
10.1	0.87	0.85	0.81	0.80	0.76	0.84	0.97	0.86	0.80	1.03	0.95	0.83
10.3	0.86	0.84	0.79	0.78	0.75	0.81	0.95	0.84	0.77	1.01	0.94	0.82
10.5	0.88	0.85	0.79	0.76	0.76	0.79	0.93	0.81	0.74	0.99	0.93	0.82
10.7	0.90	0.83	0.79	0.74	0.76	0.78	0.91	0.80	0.73	0.98	0.93	0.82
10.9	0.90	0.83	0.79	0.73	0.74	0.76	0.89	0.79	0.71	0.97	0.92	0.81
11.1	0.88	0.82	0.79	0.73	0.73	0.74	0.87	0.78	0.70	0.96	0.92	0.81
11.3	0.88	0.82	0.78	0.72	0.71	0.73	0.85	0.76	0.68	0.94	0.91	0.80
11.5	0.87	0.81	0.76	0.71	0.69	0.71	0.82	0.75	0.67	0.92	0.90	0.78
11.7	0.86	0.80	0.75	0.70	0.67	0.70	0.80	0.73	0.65	0.90	0.89	0.77
11.9	0.83	0.78	0.73	0.69	0.65	0.69	0.78	0.72	0.63	0.89	0.87	0.75
12.1	0.79	0.75	0.72	0.68	0.64	0.67	0.76	0.70	0.63	0.87	0.85	0.73
12.3	0.76	0.73	0.71	0.67	0.63	0.65	0.74	0.69	0.62	0.86	0.84	0.71
12.5	0.73	0.71	0.70	0.66	0.61	0.64	0.73	0.67	0.61	0.84	0.82	0.69
12.7	0.72	0.69	0.68	0.65	0.61	0.63	0.73	0.66	0.60	0.83	0.80	0.67
12.9	0.71	0.67	0.66	0.64	0.61	0.63	0.72	0.65	0.59	0.81	0.78	0.65
13.1	0.69	0.65	0.65	0.63	0.61	0.61	0.71	0.64	0.58	0.80	0.76	0.64
13.3	0.67	0.62	0.64	0.62	0.61	0.60	0.69	0.63	0.57	0.78	0.74	0.62
13.5	0.65	0.60	0.62	0.61	0.59	0.59	0.68	0.62	0.56	0.76	0.72	0.60
13.7	0.63	0.58	0.60	0.60	0.58	0.59	0.67	0.61	0.55	0.74	0.70	0.58
13.9	0.60	0.57	0.58	0.59	0.56	0.58	0.66	0.60	0.54	0.72	0.68	0.56
14.1	0.58	0.56	0.56	0.58	0.54	0.57	0.65	0.60	0.53	0.71	0.66	0.54
14.3	0.56	0.55	0.55	0.57	0.53	0.56	0.64	0.58	0.52	0.69	0.64	0.53
14.5	0.56	0.55	0.54	0.57	0.53	0.56	0.63	0.57	0.51	0.68	0.63	0.52
14.7	0.54	0.55	0.53	0.57	0.54	0.55	0.62	0.57	0.51	0.66	0.62	0.51
14.9	0.52	0.54	0.52	0.56	0.53	0.55	0.61	0.57	0.50	0.65	0.61	0.50
15.1	0.51	0.52	0.52	0.55	0.53	0.54	0.60	0.57	0.50	0.64	0.60	0.49
15.3	0.52	0.52	0.51	0.54	0.52	0.54	0.60	0.57	0.50	0.63	0.59	0.48
15.5	0.52	0.51	0.51	0.54	0.51	0.53	0.59	0.56	0.49	0.62	0.58	0.47
15.7	0.51	0.50	0.50	0.53	0.51	0.52	0.59	0.57	0.48	0.61	0.57	0.46
15.9	0.52	0.49	0.50	0.52	0.51	0.52	0.58	0.56	0.48	0.60	0.56	0.45
16.1	0.50	0.48	0.48	0.51	0.51	0.51	0.57	0.56	0.48	0.59	0.54	0.44
16.3	0.48	0.47	0.47	0.50	0.51	0.51	0.57	0.55	0.47	0.57	0.52	0.43
16.5	0.47	0.46	0.46	0.49	0.49	0.51	0.57	0.54	0.46	0.56	0.51	0.42
16.7	0.45	0.44	0.45	0.48	0.48	0.50	0.57	0.53	0.45	0.54	0.49	0.41
16.9	0.44	0.43	0.44	0.48	0.47	0.50	0.56	0.53	0.45	0.53	0.48	0.40
17.1	0.43	0.42	0.44	0.47	0.47	0.49	0.56	0.53	0.44	0.52	0.47	0.39
17.3	0.42	0.41	0.43	0.47	0.46	0.48	0.54	0.52	0.44	0.52	0.46	0.38
17.5	0.41	0.39	0.42	0.46	0.45	0.47	0.53	0.51	0.44	0.51	0.45	0.37
17.7	0.41	0.38	0.41	0.45	0.45	0.46	0.52	0.50	0.43	0.50	0.44	0.36
17.9	0.40	0.38	0.40	0.44	0.44	0.45	0.51	0.49	0.42	0.49	0.43	0.35
18.1	0.40	0.37	0.40	0.43	0.44	0.44	0.50	0.48	0.41	0.48	0.42	0.35
18.3	0.39	0.36	0.39	0.42	0.42	0.43	0.48	0.47	0.40	0.46	0.40	0.34
18.5	0.38	0.35	0.37	0.40	0.41	0.41	0.47	0.45	0.38	0.45	0.39	0.33

Table 2. *Cont.*

GH (km)\°	60–50° S	50–40° S	40–30° S	30–20° S	20–10° S	10° S–0°	0–10° N	10–20° N	20–30° N	30–40° N	40–50° N	50–60° N
18.7	0.36	0.35	0.36	0.38	0.39	0.39	0.45	0.43	0.37	0.43	0.38	0.32
18.9	0.35	0.34	0.35	0.36	0.37	0.38	0.43	0.41	0.36	0.41	0.37	0.31
19.1	0.35	0.33	0.34	0.34	0.35	0.37	0.41	0.39	0.34	0.40	0.35	0.30
19.3	0.34	0.33	0.32	0.33	0.34	0.36	0.40	0.38	0.32	0.39	0.34	0.29
19.5	0.34	0.32	0.31	0.32	0.32	0.35	0.38	0.36	0.31	0.37	0.33	0.29
19.7	0.33	0.31	0.30	0.30	0.31	0.33	0.37	0.35	0.29	0.36	0.32	0.28
19.9	0.33	0.29	0.28	0.29	0.30	0.32	0.36	0.33	0.28	0.35	0.31	0.27
20.1	0.33	0.28	0.27	0.28	0.29	0.31	0.35	0.32	0.27	0.34	0.30	0.27
20.3	0.31	0.28	0.26	0.27	0.28	0.30	0.34	0.31	0.26	0.32	0.29	0.26
20.5	0.30	0.27	0.26	0.26	0.27	0.28	0.32	0.29	0.25	0.31	0.28	0.25
20.7	0.29	0.26	0.25	0.25	0.26	0.27	0.31	0.28	0.24	0.30	0.27	0.24
20.9	0.29	0.26	0.24	0.24	0.26	0.26	0.30	0.27	0.23	0.29	0.26	0.24
21.1	0.28	0.26	0.23	0.23	0.25	0.25	0.29	0.26	0.23	0.28	0.26	0.23
21.3	0.27	0.25	0.23	0.23	0.24	0.24	0.28	0.25	0.22	0.27	0.25	0.23
21.5	0.27	0.24	0.22	0.22	0.23	0.24	0.28	0.25	0.21	0.26	0.24	0.22
21.7	0.25	0.23	0.21	0.21	0.22	0.23	0.26	0.24	0.21	0.25	0.23	0.21
21.9	0.25	0.22	0.21	0.21	0.21	0.23	0.26	0.23	0.20	0.24	0.23	0.21
22.1	0.24	0.22	0.20	0.20	0.21	0.22	0.24	0.22	0.20	0.24	0.22	0.20
22.3	0.23	0.22	0.19	0.20	0.20	0.21	0.24	0.21	0.19	0.23	0.22	0.20
22.5	0.23	0.21	0.19	0.19	0.20	0.21	0.23	0.21	0.18	0.22	0.21	0.19
22.7	0.23	0.21	0.18	0.18	0.19	0.20	0.22	0.20	0.18	0.21	0.20	0.19
22.9	0.22	0.21	0.18	0.18	0.18	0.19	0.21	0.20	0.17	0.21	0.20	0.18
23.1	0.21	0.21	0.17	0.17	0.17	0.19	0.21	0.19	0.17	0.20	0.19	0.18
23.3	0.21	0.20	0.17	0.17	0.17	0.19	0.20	0.19	0.17	0.20	0.19	0.18
23.5	0.21	0.20	0.17	0.17	0.16	0.18	0.20	0.19	0.16	0.19	0.18	0.17
23.7	0.21	0.19	0.16	0.16	0.16	0.18	0.19	0.18	0.16	0.19	0.18	0.17
23.9	0.20	0.18	0.16	0.16	0.16	0.17	0.18	0.17	0.15	0.18	0.17	0.16
24.1	0.19	0.18	0.15	0.15	0.15	0.17	0.18	0.17	0.15	0.17	0.17	0.16
24.3	0.18	0.17	0.14	0.14	0.15	0.16	0.17	0.16	0.14	0.17	0.16	0.15
24.5	0.18	0.16	0.14	0.14	0.14	0.15	0.17	0.16	0.14	0.16	0.16	0.15
24.7	0.17	0.15	0.13	0.13	0.13	0.14	0.16	0.15	0.13	0.15	0.15	0.14
24.9	0.16	0.15	0.12	0.13	0.13	0.14	0.15	0.14	0.13	0.15	0.14	0.14
25.1	0.16	0.14	0.12	0.12	0.12	0.13	0.14	0.13	0.12	0.14	0.14	0.13

4. Discussion and Conclusions

This study evaluates the quality of TM RO bending angle and refractivity retrievals from China's first commercial low Earth orbit meteorological constellation. In addition to ERA5 reanalysis and global radiosonde observations, the internationally recognized, high-quality COSMIC-2 RO dataset is used as an RO-based reference to further assess the consistency of TM RO retrievals. Comparing TM and COSMIC-2 RO data yields a more comprehensive assessment of TM RO data. This study also provides the first systematic evaluation of TM RO observation errors using the 3CH method.

The results show that TM RO refractivity and bending angle retrievals are in good agreement with the reference datasets in the upper troposphere and lower stratosphere, demonstrating their high quality. In the 8–30 km height range, the bending angle biases of TM relative to ERA5 and COSMIC-2 are within ±0.19% and ±0.37%, respectively, while the bias relative to radiosonde data remains within ±0.40% over 8–25 km. For refractivity, the biases are within ±0.09% and ±0.14% relative to ERA5 and COSMIC-2, and within ±0.21% relative to radiosonde data. These results demonstrate the potential of TM GNSS RO data for weather forecasting and climate applications in the upper troposphere and

lower stratosphere. However, TM data exhibit positive refractivity and bending angle biases below 8 km relative to ERA5, radiosonde, and COSMIC-2, with maximum biases of 0.71% and 1.86%, respectively. These positive lower tropospheric biases may be related to retrieval processing differences, residual multipath effects, local spectral asymmetry in RO signal noise, penetration depth differences, or collocation and representativeness errors. Further analyses are needed to identify the dominant source of these biases.

The observation errors estimated using the 3CH method show clear vertical and latitudinal dependence for both TM bending angle and refractivity. Observation errors in the tropics ($\pm 30^{\circ}$ latitude) are generally larger than those in the middle and high latitudes. These TM-specific observation error estimates provide a quantitative basis for specifying observation error in future numerical weather prediction data assimilation. Because the 3CH method assumes mutually independent dataset errors, the estimated values should be interpreted as effective observation errors rather than pure instrument measurement errors.

Previous forecast impact studies have shown that GNSS RO data make substantial contributions to numerical weather prediction, especially in data-sparse regions and the tropics. The emergence of commercial RO missions provides new opportunities to improve atmospheric analyses and forecasts. The quality assessment and observation error estimates presented in this study provide a useful basis for developing TM RO quality control procedures and observation error specifications. In future work, TM RO data will be assimilated into numerical weather prediction systems to investigate the impact of commercial RO observations on forecasts, particularly for high-impact weather systems such as tropical cyclones. Further evaluations over longer time periods and different seasons are also needed to examine the stability of TM RO data quality and observation error characteristics.

Author Contributions: Conceptualization, S.Y.; data curation, L.W. and B.Y.; formal analysis, L.W. and S.Y.; funding acquisition, S.Y.; investigation, L.W.; methodology, S.Y. and L.H.; project administration, S.Y.; resources, S.Y.; writing—original draft, L.W.; writing—review and editing, S.Y. All authors have read and agreed to the published version of the manuscript.

Funding: This work was supported by the project of Civil Aerospace Preliminary Research (D010404), the Key Research and Development Program of Guangxi (GuiKe AB25069131), and the Postgraduate Research & Practice Innovation Program of Jiangsu Province (KYCX25_1591).

Data Availability Statement: The COSMIC-2 RO data used in this study can be downloaded at https://data.cosmic.ucar.edu/gnss-ro/cosmic2/nrt/level2/2022/ (accessed on 10 March 2025). The ECMWF ERA5 reanalysis data used in this study can be downloaded at https://apps.ecmwf.int/data-catalogues/era5/?stream=oper&levtype=ml&expver=1&month=jan&year=2022&type=an&class=ea (accessed on 11 March 2025). The NCEP FNL data used in this study can be downloaded at https://gdex.ucar.edu/datasets/d083002/dataaccess/ (accessed on 12 March 2025). The NOAA IGRA data used in this study can be downloaded at https://www.ncei.noaa.gov/products/weather-balloon/integrated-global-radiosonde-archive (accessed on 15 March 2025).

Conflicts of Interest: The authors declare no conflicts of interest.

References

1. Ware, R.; Exner, M.; Feng, D.; Gorbunov, M.; Hardy, K.; Herman, B.; Trenberth, K. GPS sounding of the atmosphere from low Earth orbit: Preliminary results. *Bull. Am. Meteorol. Soc.* **1996**, *77*, 19–40. [CrossRef]
2. Kuo, Y.-H.; Wee, T.-K.; Sokolovskiy, S.; Rocken, C.; Schreiner, W.; Hunt, D.; Anthes, R.A. Inversion and error estimation of GPS radio occultation data. *J. Meteorol. Soc. Jpn. Ser. II* **2004**, *82*, 507–531. [CrossRef]
3. Schreiner, W.S.; Weiss, J.P.; Anthes, R.A.; Braun, J.; Chu, V.; Fong, J.; Hunt, D.; Kuo, Y.-H.; Meehan, T.; Serafino, W.; et al. COSMIC-2 radio occultation constellation: First results. *Geophys. Res. Lett.* **2020**, *47*, e2019GL086841. [CrossRef]
4. Holmlund, K.; Counet, P.; Martinez Fadrique, F.; Schmid, A.; Bojkov, B.; Munro, R.; Grandell, J.; Obligis, E. The EUMETSAT satellite programmes and data services. *J. Eur. Meteorol. Soc.* **2025**, *2*, 100005. [CrossRef]

5. von Engeln, A.; Andres, Y.; Marquardt, C.; Sancho, F. GRAS radio occultation on-board of Metop. *Adv. Space Res.* **2011**, *47*, 336–347. [CrossRef]
6. Cai, Y.; Bai, W.; Wang, X.; Sun, Y.; Du, Q.; Zhao, D.; Meng, X.; Liu, C.; Xia, J.; Wang, D.; et al. In-orbit performance of GNOS on-board FY3-C and the enhancements for FY3-D satellite. *Adv. Space Res.* **2017**, *60*, 2812–2821. [CrossRef]
7. He, Y.; Zhang, S.; Guo, S.; Wu, Y. Quality Assessment of the Atmospheric Radio Occultation Profiles from FY-3E/GNOS-II BDS and GPS Measurements. *Remote Sens.* **2023**, *15*, 5313. [CrossRef]
8. Kursinski, E.R.; Hajj, G.A.; Schofield, J.T.; Linfield, R.P.; Hardy, K.R. Observing Earth's atmosphere with radio occultation measurements using the Global Positioning System. *J. Geophys. Res. Atmos.* **1997**, *102*, 23429–23465. [CrossRef]
9. Gleisner, H.; Ringer, M.A.; Healy, S.B. Monitoring global climate change using GNSS radio occultation. *npj Clim. Atmos. Sci.* **2022**, *5*, 6. [CrossRef]
10. Cucurull, L.; Derber, J.C.; Treadon, R.; Purser, R.J. Assimilation of global positioning system radio occultation observations into NCEP's global data assimilation system. *Mon. Weather Rev.* **2007**, *135*, 3174–3193. [CrossRef]
11. Ma, Z.; Kuo, Y.-H.; Ralph, F.M.; Neiman, P.J.; Wick, G.A.; Sukovich, E.; Wang, B. Assimilation of GPS radio occultation data for an intense atmospheric river with the NCEP regional GSI system. *Mon. Weather Rev.* **2011**, *139*, 2170–2183. [CrossRef]
12. Ho, S.-P.; Zhou, X.; Shao, X.; Chen, Y.; Jing, X.; Miller, W. Using the commercial GNSS RO Spire data in the neutral atmosphere for climate and weather prediction studies. *Remote Sens.* **2023**, *15*, 4836. [CrossRef]
13. Yue, H.; Fu, N.; Li, F.; Cheng, Y.; Wu, M.; Guo, P.; Dong, W.; Hu, X.; Wang, F. The Yunyao LEO satellite constellation: Occultation results of the neutral atmosphere using multi-system global navigation satellites. *Remote Sens.* **2025**, *17*, 2851. [CrossRef]
14. Yang, S.; Zou, X. Assimilating Tianmu-1 RO data from a 23-satellite constellation to enhance the track forecasts of Typhoon Gaemi (2024). *Geophys. Res. Lett.* **2025**, *52*, e2025GL115679. [CrossRef]
15. Liu, X.; Bu, J.; Zuo, X.; Wang, Z.; Wang, Q.; Wang, Q.; He, X. Performance validation of sea surface wind speed retrieval algorithms and products from the Chinese Tianmu-1 constellation GNSS-R: First results on comparison with other wind speed products. *IEEE J. Sel. Top. Appl. Earth Obs. Remote Sens.* **2025**, *18*, 5189–5203. [CrossRef]
16. Steiner, A.K.; Ladstädter, F.; Ao, C.O.; Gleisner, H.; Ho, S.-P.; Hunt, D.; Schmidt, T.; Foelsche, U.; Kirchengast, G.; Kuo, Y.-H.; et al. Consistency and structural uncertainty of multi-mission GPS radio occultation records. *Atmos. Meas. Tech.* **2020**, *13*, 2547–2575. [CrossRef]
17. Chen, S.-Y.; Liu, C.-Y.; Huang, C.-Y.; Hsu, S.-C.; Li, H.-W.; Lin, P.-H.; Cheng, J.-P.; Huang, C.-Y. An analysis study of FORMOSAT 7/COSMIC-2 radio occultation data in the troposphere. *Remote Sens.* **2021**, *13*, 717. [CrossRef]
18. Durre, I.; Vose, R.S.; Wuertz, D.B. Overview of the Integrated Global Radiosonde Archive. *J. Clim.* **2006**, *19*, 53–68. [CrossRef]
19. Fjeldbo, G.; Kliore, A.J.; Eshleman, V.R. The neutral atmosphere of Venus as studied with the Mariner V Radio Occultation experiments. *Astron. J.* **1971**, *76*, 123. [CrossRef] [PubMed]
20. Gilpin, S.; Anthes, R.; Sokolovskiy, S. Sensitivity of Forward-Modeled Bending Angles to Vertical Interpolation of Refractivity for Radio Occultation Data Assimilation. *Mon. Weather Rev.* **2019**, *147*, 269–289. [CrossRef]
21. Zou, X.; Zeng, Z. A quality control procedure for GPS radio occultation data. *J. Geophys. Res.* **2006**, *111*, D02112. [CrossRef]
22. Anthes, R.A.; Rieckh, T. Estimating observation and model error variances using multiple data sets. *Atmos. Meas. Tech.* **2018**, *11*, 4239–4260. [CrossRef]
23. Xu, X.; Zou, X. Estimating GPS radio occultation observation error standard deviations over China using the three-cornered hat method. *Q. J. R. Meteorol. Soc.* **2021**, *147*, 647–659. [CrossRef]
24. Syndergaard, S. On the ionosphere calibration in GPS radio occultation measurements. *Radio Sci.* **2000**, *35*, 865–883. [CrossRef]
25. Steiner, A.K.; Kirchengast, G. Error analysis for GNSS radio occultation data based on ensembles of profiles from end-to-end simulations. *J. Geophys. Res.* **2005**, *110*, D05251. [CrossRef]
26. Mannucci, A.J.; Ao, C.O.; Pi, X.; Iijima, B.A. The impact of large scale ionospheric structure on radio occultation retrievals. *Atmos. Meas. Tech.* **2011**, *4*, 2837–2850. [CrossRef]
27. Gorbunov, M.; Kirchengast, G.; Lauritsen, K.B. Generalized canonical transform method for radio occultation sounding with improved retrieval in the presence of horizontal gradients. *Atmos. Meas. Tech.* **2021**, *14*, 853–867. [CrossRef]
28. Wang, L.; Yang, S. Planetary Boundary Layer Structure as the Primary Driver of Simulated Impact Multipath in GNSS Radio Occultation. *Remote Sens.* **2026**, *18*, 352. [CrossRef]
29. Ao, C.O.; Meehan, T.K.; Hajj, G.A.; Mannucci, A.J.; Beyerle, G. Lower troposphere refractivity bias in GPS occultation retrievals. *J. Geophys. Res. Atmos.* **2003**, *108*, 4577. [CrossRef]
30. Feng, X.; Xie, F.; Ao, C.O.; Anthes, R.A. Ducting and biases of GPS radio occultation bending angle and refractivity in the moist lower troposphere. *J. Atmos. Ocean. Technol.* **2020**, *37*, 1013–1025. [CrossRef]
31. Sokolovskiy, S.V. Effect of superrefraction on inversions of radio occultation signals in the lower troposphere. *Radio Sci.* **2003**, *38*, 1058. [CrossRef]
32. Xie, F.; Wu, D.L.; Ao, C.O.; Kursinski, E.R.; Mannucci, A.J.; Syndergaard, S. Super-refraction effects on GPS radio occultation refractivity in marine boundary layers. *Geophys. Res. Lett.* **2010**, *37*, L11805. [CrossRef]

33. Yang, S.; Zou, X. Relationships of along-the-track local variations of GPS RO impact parameter to strong local vertical gradient of wet refractivity in the tropics. *Sci. China Earth Sci.* **2021**, *64*, 2015–2026. [CrossRef]
34. Yang, S.; Zou, X.; Anthes, R. Raytracing Simulated GPS Radio Wave Propagation Paths Experiencing Large Disturbances When Going through the Top of the Sub-Cloud Layer. *Remote Sens.* **2021**, *13*, 4693. [CrossRef]
35. Sokolovskiy, S.; Rocken, C.; Schreiner, W.; Hunt, D. On the uncertainty of radio occultation inversions in the lower troposphere. *J. Geophys. Res. Atmos.* **2010**, *115*, D22111. [CrossRef]
36. Qi, X.; Yang, S.; He, L. Investigating Tropical Cyclone Warm Core and Boundary Layer Structures with Constellation Observing System for Meteorology, Ionosphere, and Climate 2 Radio Occultation Data. *Remote Sens.* **2024**, *16*, 4257. [CrossRef]

Disclaimer/Publisher's Note: The statements, opinions and data contained in all publications are solely those of the individual author(s) and contributor(s) and not of MDPI and/or the editor(s). MDPI and/or the editor(s) disclaim responsibility for any injury to people or property resulting from any ideas, methods, instructions or products referred to in the content.